Mechanics of Advanced Materials and Structures

ISSN: (Print) (Online) Journal homepage: www.tandfonline.com/journals/umcm20

Energy absorption and frequency analysis of the nanocomposites reinforced car's hood under airflow pressure

Wenrong Yin, Hao Zhang, Mohammed A. El-Meligy & Mehdi Tlija

To cite this article: Wenrong Yin, Hao Zhang, Mohammed A. El-Meligy & Mehdi Tlija (17 Sep 2024): Energy absorption and frequency analysis of the nanocomposites reinforced car's hood under airflow pressure, Mechanics of Advanced Materials and Structures, DOI: 10.1080/15376494.2024.2393733

To link to this article: https://doi.org/10.1080/15376494.2024.2393733

Published online: 17 Sep 2024.

https://doi.org/10.1080/15376494.2024.2393733

Taylor & Francis
Taylor & Francis Group

ORIGINAL ARTICLE

Check for updates

Energy absorption and frequency analysis of the nanocomposites reinforced car's hood under airflow pressure

Wenrong Yin[a], Hao Zhang[b], Mohammed A. El-Meligy[c,d], and Mehdi Tlija[e]

[a]Development Planning Office, Shandong Huayu University of Technology, Dezhou, China; [b]Physical Fitness Testing Center, Shandong Huayu University of Technology, Dezhou, China; [c]Jadara University Research Center, Jadara University, Jordan; [d]Applied Science Research Center, Applied Science Private University, Amman, Jordan; [e]Department of Industrial Engineering, College of Engineering, King Saud University, Riyadh, Saudi Arabia

ABSTRACT
This study focuses on the energy absorption and frequency analysis of a car's hood reinforced with graphene platelets nanocomposites under airflow pressure. The integration of nanocomposites aims to enhance the mechanical properties and energy absorption capacity of the hood, crucial for improving vehicle safety and performance. We investigate the dynamic response of the hood structure subjected to varying airflow pressures, utilizing advanced computational models to simulate real-world conditions. The analysis employs numerical method to evaluate the frequency characteristics and energy absorption efficiency of the nanocomposite-reinforced hood. Results indicate significant improvements in both energy absorption and frequency response, highlighting the potential of nanocomposite materials to optimize the dynamic performance and structural resilience of automotive components. This research provides valuable insights into the design and application of nanocomposite materials in the automotive industry, promoting the development of safer and more efficient vehicles. The findings suggest that incorporating nanocomposites in car hoods can lead to superior impact resistance and vibration dampening, which are critical for maintaining the integrity and functionality of the vehicle under operational conditions.

ARTICLE HISTORY
Received 30 July 2024
Accepted 13 August 2024

KEYWORDS
Energy absorption; vibrational analysis; GPLs; car's hood; airflow pressure

1. Introduction

Advanced composite structures are integral to modern engineering, offering unmatched performance in various applications [1–3]. These materials, comprising a combination of two or more constituent materials with different properties, result in composites that possess superior strength, stiffness, and lightweight characteristics [4, 5]. Unlike traditional materials such as metals, composites can be tailored to meet specific requirements by altering the composition, orientation, and volume fraction of their constituents [6, 7]. This flexibility allows for the design of structures with optimized performance for demanding environments. One of the primary benefits of advanced composites is their high strength-to-weight ratio, making them ideal for aerospace, automotive, and sporting goods industries [8, 9]. In aerospace, for instance, the use of composite materials has significantly reduced aircraft weight, leading to improved fuel efficiency and reduced emissions. Similarly, in the automotive industry, composites contribute to lighter, more fuel-efficient vehicles without compromising safety or performance [10–12]. Nanocomposites, a subset of advanced composites, incorporate nanoscale fillers to further enhance mechanical, thermal, and electrical properties [13–15]. These materials are gaining attention for their potential in next-generation electronics, medical devices, and energy storage systems [16, 17]. The integration of nanomaterials such as carbon nanotubes, graphene, and nanoclays into polymer matrices has opened new avenues for research and development in material science [18]. Furthermore, the development of smart composites that can sense, react, and adapt to their environment is revolutionizing the field [19]. These materials can monitor structural health, self-heal minor damages, and change properties in response to external stimuli, enhancing safety and reliability [20, 21]. Manufacturing processes for advanced composites are also evolving, with techniques like automated fiber placement, resin transfer molding, and additive manufacturing improving production efficiency and quality [22]. These advancements are making composite materials more accessible and cost-effective for a wider range of applications. In conclusion, advanced composite structures represent a significant leap forward in material science and engineering [23, 24]. Their unique properties and adaptability are driving innovation across various industries, from aerospace to renewable energy [25]. As research and technology continue to advance, the potential for even more sophisticated and sustainable composite materials is vast, promising a future where high-performance, lightweight, and intelligent structures become the norm [26].

Shear deformation theories are crucial for engineers because they provide a more accurate representation of the

CONTACT Wenrong Yin 421142717@qq.com Development Planning Branch, Shandong Huayu University of Technology, Dezhou, China.

behavior of structural elements under load [27]. Unlike classical beam theories, which assume that plane sections remain plane and perpendicular to the neutral axis, shear deformation theories account for the effects of shear strains, which become significant in thick beams and high-stress applications [28]. This leads to better predictions of deflections, stresses, and natural frequencies, essential for designing safe and efficient structures [29]. By incorporating shear deformation, these theories help engineers design structures that can withstand higher loads and operate more effectively under various conditions. This is particularly important in advanced composite materials, where shear effects can greatly influence performance. Engineers use shear deformation theories to optimize material usage, reduce weight, and improve the overall structural integrity of beams, plates, and shells [30]. Furthermore, these theories are vital for understanding and predicting failure modes, such as shear buckling and delamination in composites [31]. They also enhance the accuracy of finite element models, which are widely used in engineering analysis and design [32]. Ultimately, shear deformation theories contribute to the development of innovative and reliable engineering solutions across multiple industries [33].

Modeling complex systems is of paramount importance for engineers, as it provides a comprehensive understanding of how various components interact within a system [34, 35]. By creating accurate models, engineers can predict the behavior of these systems under different conditions, enabling them to design more efficient, reliable, and cost-effective solutions [36, 37]. Complex systems often involve numerous interdependent variables and dynamic processes, making analytical solutions impractical or impossible [38, 39]. Therefore, computational modeling becomes essential for capturing these intricacies [40, 41]. One of the primary benefits of modeling complex systems is the ability to perform simulations that replicate real-world conditions [42, 43]. This allows engineers to test different scenarios and evaluate the performance of a system without the need for expensive and time-consuming physical prototypes [44, 45]. For example, in aerospace engineering, modeling the aerodynamics of an aircraft can help optimize its design for fuel efficiency and stability before a single component is manufactured [46, 47]. Moreover, modeling aids in identifying potential issues and vulnerabilities within a system [48, 49]. By understanding how different components interact, engineers can anticipate failure points and devise strategies to mitigate risks [50, 51]. This proactive approach enhances the safety and reliability of engineering projects, whether it is a bridge, a power grid, or a communication network [52, 53]. Complex system modeling is also critical for optimizing resource allocation and improving efficiency [20, 21]. In manufacturing, for instance, models can simulate production processes to identify bottlenecks and optimize workflow, leading to reduced costs and increased productivity [54, 55]. Similarly, in the energy sector, modeling can help in the design and management of smart grids, ensuring efficient distribution and utilization of resources [56, 57]. Furthermore, models provide a valuable tool for decision-making and strategic planning [58, 59]. They offer a way to visualize the impact of different choices and policies, enabling engineers and stakeholders to make informed decisions [60]. This is particularly important in large-scale infrastructure projects, where the consequences of decisions can be far-reaching and costly [61]. In addition, modeling supports innovation by enabling the exploration of new concepts and technologies [62]. Engineers can use models to test the feasibility of cutting-edge ideas, such as advanced materials or novel structural designs, accelerating the development and implementation of innovative solutions [63].

This research focuses on the energy absorption and frequency analysis of a graphene platelets (GPLs) nanocomposites-reinforced automobile hood under airflow pressure. The goal of integrating nanocomposites is to improve the hood's mechanical characteristics and energy-absorbing ability, which are essential for raising car performance and safety. We study the dynamic behavior of the hood structure under different airflow pressures by simulating real-world situations using sophisticated computer models. The investigation uses a computational approach to assess the energy absorption efficiency and frequency characteristics of the hood reinforced with nanocomposite. Significant gains in energy absorption and frequency responsiveness are shown by the results, underscoring the potential of nanocomposite materials to maximize the structural robustness and dynamic performance of automotive components. This study advances the creation of safer and more effective automobiles by offering insightful information on the development and use of nanocomposite materials in the automotive sector. According to the research, adding nanocomposites to car hoods may improve their impact resistance and vibration damping—two qualities that are essential for preserving the vehicle's structural integrity and operating capabilities.

2. Effective material properties of GPLRCs

A multilayer doubly curved panel made of completely bonded GPLRC layers, is shown in Figure 1.

The GPLRC layer is thought to be composed of a blend of evenly distributed, randomly oriented rectangular GPLs and an isotropic polymer matrix. As such, each GPLRC layer alone is isotropically homogenous, and its effective Young's modulus may be calculated using the micromechanics model of Halpin and Tsai [64]

$$E = \frac{3}{8}\frac{1+\xi_L\eta_L V_{GPL}}{1-\eta_L V_{GPL}} \times E_m + \frac{5}{8}\frac{1+\xi_T\eta_T V_{GPL}}{1-\eta_T V_{GPL}} \times E_m, \qquad (1)$$

where parameters η_L and η_T take the following forms:

$$\eta_L = \frac{(E_{GPL}/E_m)-1}{(E_{GPL}/E_m)+\xi_L}, \eta_T = \frac{(E_{GPL}/E_m)-1}{(E_{GPL}/E_m)+\xi_T}. \qquad (2)$$

where the Young's moduli of the GPL and matrix are, respectively, E_{GPL} and E_m. The volume proportion of GPL nanofillers is denoted by V_{GPL}. It should be noted that the geometry and dimension of the GPL are taken into

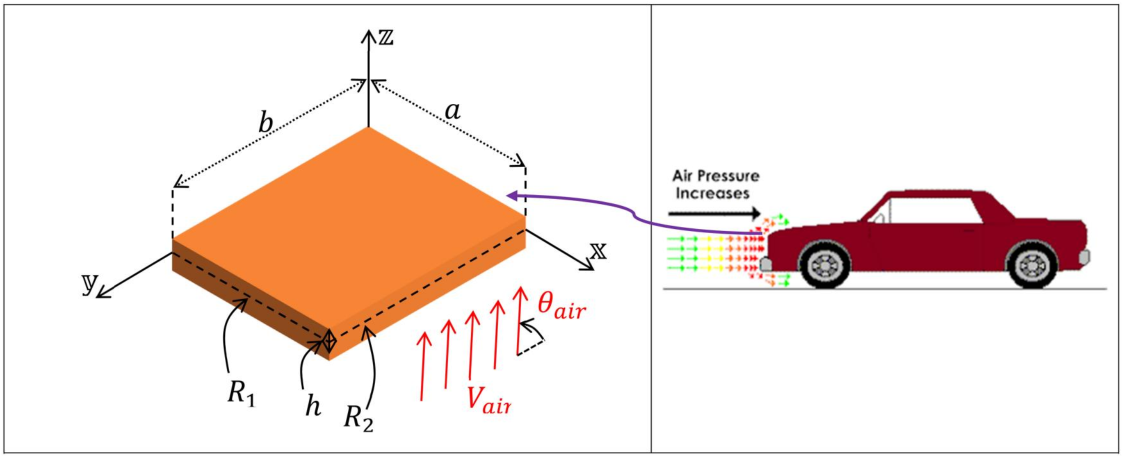

Figure 1. The GPLRC doubly curved panel's shape and coordinate system under airflow pressure.

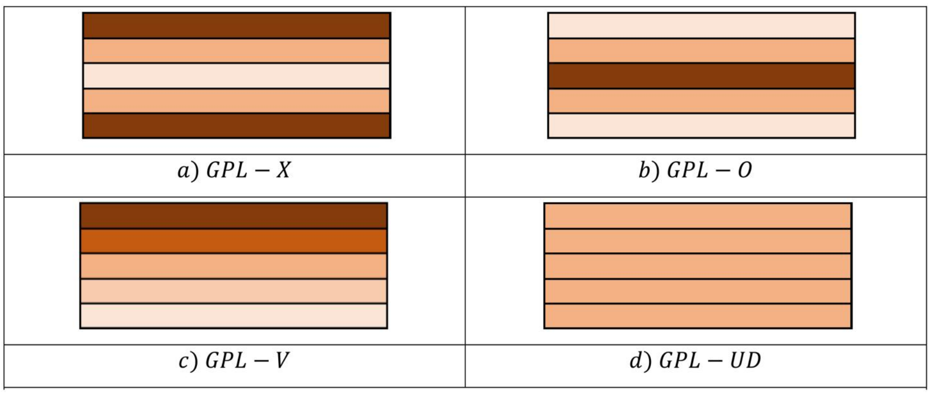

Figure 2. GPL distribution patterns over the GPLRC double curved panel's thickness.

consideration by Eq. (1) *via* the geometry factors ξ_L and ξ_T which are defined by Halpin Affdl and Kardos [64].

$$\xi_L = 2(a_{GPL}/t_{GPL}), \xi_T = 2(b_{GPL}/t_{GPL}). \tag{3}$$

The length, breadth, and thickness of GPLs are denoted by the variables a_{GPL}, b_{GPL}, and t_{GPL} accordingly ξ_L may be rewritten in this case as

$$\xi = 2(\alpha_{GPL}/b_{GPL}) \times (b_{GPL}/t_{GPL}). \tag{4}$$

in which α_{GPL}/b_{GPL} and b_{GPL}/t_{GPL} are GPL aspect ratio and width-to-thickness ratio, respectively. The GPLRC's mass density (ρ) and Poisson's ratio (ν) may be expressed using the rule of mixing.

$$\rho = \rho_m V_m + \rho_{GPL} V_{GPL}, \tag{5a}$$

$$\nu = \nu_m V_m + \nu_{GPL} V_{GPL}, \tag{5b}$$

where ρ_{GPL} and ρ_m are mass densities, with the subscript "GPL" and "m" referring to the GPLs and matrix, respectively. ν_{GPL} and ν_m are Poisson's ratios; the volume fractions V_{GPL} and V_m are related by

$$V_m + V_{GPL} = 1. \tag{6}$$

The thickness direction of the doubly curved panel in Figure 2 displays the uniform (U) and functionally graded (X, O) distributions of GPL nanofillers. The darker color indicates a larger concentration of GPLs inside the layer. In the uniform distribution, GPL-UD corresponds to an isotropic homogeneous doubly curved panel since the GPL content is consistent across all levels. However, in the functionally graded distributions, the GPL weight fraction changes layer to layer such that, in a GPL-X doubly curved panel, the top and bottom layers are both GPL rich; in a GPL-O doubly curved panel, on the other hand, the intermediate layers are GPL rich. For GPL-V, the GPL volume percentage rises steadily from the bottom surface to the top surface.

It is expected that the multilayer GPLRC doubly curved panel has an even number of layers without losing generality. For each of the four GPL distribution patterns shown in Figure 2, the GPL volume percentage of the kth layer is given as

$$\text{GPL-UD}: V_{GPL}^{(k)} = V_{GPL}^{*}, \tag{7a}$$

$$\text{GPL-X}: V_{GPL}^{(k)} = 2V_{GPL}^{*}|2k - N_L - 1|/N_L, \tag{7b}$$

$$\text{GPL-O}: V_{GPL}^{(k)} = 2V_{GPL}^{*}(1 - |2k - N_L - 1|/N_L), \tag{7c}$$

$$\text{GPL-V}: V_{GPL}^{(k)} = V_{GPL}^{*}((2k - 1)/N_L), \tag{7d}$$

where $k = 1, 2, \ldots, N_L$, and N_L is the total number of layers in the beam, and V_{GPL}^{*} is the overall GPL volume percentage, which is calculated by

$$V_{\mathrm{GPL}}^{*}=\frac{W_{\mathrm{GPL}}}{W_{\mathrm{GPL}}+(\rho_{\mathrm{GPL}}/\rho_{\mathrm{m}})(1-W_{\mathrm{GPL}})}. \tag{8}$$

where W_{GPL} is the weight fraction of GPL overall for the whole doubly curved panel. The total volume fractions of GPLs in the GPL-UD, GPL-X, GPL-O, and GPL-V doubly curved panels are the same, as can be shown from Eqs. (7a)–(7c).

3. Vibration theoretical model

In the present work, the governing equations are derived using the FSDT and then used to analyze the vibration behavior of the GPLRC doubly curved panel under airflow pressure. The displacement field of the shell structures is shown as follows [65]:

$$\mathbb{U}(\mathbb{x},\mathbb{y},\mathbb{z},t)=\mathbb{u}(\mathbb{x},\mathbb{y},t)+\mathbb{z}\phi_{\mathbb{x}}(\mathbb{x},\mathbb{y},t), \tag{9a}$$

$$\mathbb{V}(\mathbb{x},\mathbb{y},\mathbb{z},t)=\mathbb{v}(\mathbb{x},\mathbb{y},t)+\mathbb{z}\phi_{\mathbb{y}}(\mathbb{x},\mathbb{y},t), \tag{9b}$$

$$\mathbb{W}(\mathbb{x},\mathbb{y},\mathbb{z},t)=\mathbb{w}(\mathbb{x},\mathbb{y},t). \tag{9c}$$

The center surface displacement along the x-axis inside the plane is represented by the variable $\mathbb{u}$, while the displacements along the y- and z-axes are represented by the variables $\mathbb{v}$ and $\mathbb{w}$, respectively. Additionally, the rotational displacement components around the $\mathbb{y}$-axis and $\mathbb{x}$-axis are indicated by the variables $\phi_{\mathbb{x}}$ and $\phi_{\mathbb{y}}$, respectively. Shear and transverse strain-displacement interactions may be represented as a representation of any position displacement field:

$$\begin{Bmatrix}\varepsilon_{\mathbb{x}}\\ \varepsilon_{\mathbb{y}}\\ \gamma_{\mathbb{xy}}\end{Bmatrix}=\begin{Bmatrix}\dfrac{\partial\mathbb{u}}{\partial\mathbb{x}}+\dfrac{\mathbb{w}}{R_1}+z\dfrac{\partial\phi_{\mathbb{x}}}{\partial\mathbb{x}}\\ \dfrac{\partial\mathbb{v}}{\partial\mathbb{y}}+\dfrac{\mathbb{w}}{R_2}+z\dfrac{\partial\phi_{\mathbb{y}}}{\partial\mathbb{y}}\\ \dfrac{\partial\mathbb{u}}{\partial\mathbb{y}}+\dfrac{\partial\mathbb{v}}{\partial\mathbb{x}}+z\dfrac{\partial\phi_{\mathbb{x}}}{\partial\mathbb{y}}+z\dfrac{\partial\phi_{\mathbb{y}}}{\partial\mathbb{x}}\end{Bmatrix},\quad \begin{Bmatrix}\gamma_{\mathbb{xz}}\\ \gamma_{\mathbb{yz}}\end{Bmatrix}=\begin{Bmatrix}\phi_{\mathbb{x}}+\dfrac{\partial\mathbb{w}}{\partial\mathbb{x}}-\dfrac{\mathbb{u}}{R_1}\\ \phi_{\mathbb{y}}+\dfrac{\partial\mathbb{w}}{\partial\mathbb{y}}-\dfrac{\mathbb{v}}{R_2}\end{Bmatrix}. \tag{10}$$

where the shear components of strain are indicated by $\gamma_{\mathbb{xy}}$, $\gamma_{\mathbb{xz}}$, and $\gamma_{\mathbb{yz}}$, while the normal components of strain are represented by $\varepsilon_{\mathbb{x}}$ and $\varepsilon_{\mathbb{y}}$. Additionally, the relationship between stress and strain in the GPLRC doubly curved panel is explained by Hooke's law:

$$\begin{Bmatrix}\sigma_{\mathbb{x}}\\ \sigma_{\mathbb{y}}\\ \tau_{\mathbb{xy}}\end{Bmatrix}=\begin{bmatrix}Q_{11}&Q_{12}&0\\ Q_{12}&Q_{22}&0\\ 0&0&Q_{66}\end{bmatrix}\begin{Bmatrix}\varepsilon_{\mathbb{x}}\\ \varepsilon_{\mathbb{y}}\\ \gamma_{\mathbb{xy}}\end{Bmatrix},\quad \begin{Bmatrix}\tau_{\mathbb{yz}}\\ \tau_{\mathbb{xz}}\end{Bmatrix}=\begin{bmatrix}Q_{44}&0\\ 0&Q_{55}\end{bmatrix}\begin{Bmatrix}\gamma_{\mathbb{yz}}\\ \gamma_{\mathbb{xz}}\end{Bmatrix}. \tag{11}$$

Furthermore, the stiffness coefficient used in Eq. (11) may be expressed as follows:

$$Q_{11}=Q_{22}=\frac{E}{1-\nu^2},Q_{12}=\frac{\nu E}{1-\nu^2},Q_{66}=Q_{44}=Q_{55}=\frac{E}{2(1+\nu)}. \tag{12}$$

According to Hamilton principle [65], we have:

$$\int_0^t\delta(U+V-K)dt=0. \tag{13}$$

where δ is the variational operator. The GPLRC doubly curved panel's change in strain energy, δU, may be defined as follows:

$$\begin{aligned}\delta U=&\int_{\mathbb{V}}(\sigma_{\mathbb{x}}\delta\varepsilon_{\mathbb{x}}+\sigma_{\mathbb{y}}\delta\varepsilon_{\mathbb{y}}+\tau_{\mathbb{xy}}\delta\gamma_{\mathbb{xy}}+\tau_{\mathbb{yz}}\delta\gamma_{\mathbb{yz}}\\&+\tau_{\mathbb{xz}}\delta\gamma_{\mathbb{xz}})d\mathbb{V}\\=&\int_A\Bigg(\mathbb{N}_{\mathbb{x}}\left(\frac{\partial\delta\mathbb{u}}{\partial\mathbb{x}}+\frac{\delta\mathbb{w}}{R_1}\right)+\mathbb{N}_{\mathbb{y}}\left(\frac{\partial\delta\mathbb{v}}{\partial\mathbb{y}}+\frac{\delta\mathbb{w}}{R_2}\right)\\&+\mathbb{N}_{\mathbb{xy}}\left(\frac{\partial\delta\mathbb{u}}{\partial\mathbb{x}}+\frac{\partial\delta\mathbb{v}}{\partial\mathbb{y}}\right)+\mathbb{M}_{\mathbb{x}}\frac{\partial\delta\phi_{\mathbb{x}}}{\partial\mathbb{x}}+\mathbb{M}_{\mathbb{y}}\frac{\partial\delta\phi_{\mathbb{y}}}{\partial\mathbb{y}}\\&+\mathbb{M}_{\mathbb{xy}}\left(\frac{\partial\delta\phi_{\mathbb{x}}}{\partial\mathbb{x}}+\frac{\partial\delta\phi_{\mathbb{y}}}{\partial\mathbb{y}}\right)+\mathbb{Q}_{\mathbb{xz}}\left(\delta\phi_{\mathbb{x}}+\frac{\partial\delta\mathbb{w}}{\partial\mathbb{x}}-\frac{\delta\mathbb{u}}{R_1}\right)\\&+\mathbb{Q}_{\mathbb{yz}}\left(\delta\phi_{\mathbb{y}}+\frac{\partial\delta\mathbb{w}}{\partial\mathbb{y}}-\frac{\delta\mathbb{v}}{R_2}\right)\Bigg)dA.\end{aligned} \tag{14}$$

In the doubly curved panel, the variables $\mathbb{N}_{\mathbb{x}},\mathbb{N}_{\mathbb{y}}$, and $\mathbb{N}_{\mathbb{xy}}$ represent the membrane forces, $\mathbb{M}_{\mathbb{x}},\mathbb{M}_{\mathbb{y}}$, and $\mathbb{M}_{\mathbb{xy}}$ represent the bending moments, and $\mathbb{Q}_{\mathbb{xz}},\mathbb{Q}_{\mathbb{yz}}$ represent the shear forces. These variables may be represented using the following formulas:

$$\begin{Bmatrix}\mathbb{N}_{\mathbb{x}}\\ \mathbb{N}_{\mathbb{y}}\\ \mathbb{N}_{\mathbb{xy}}\end{Bmatrix}=\int_{-h/2}^{h/2}\begin{Bmatrix}\sigma_{\mathbb{x}}\\ \sigma_{\mathbb{y}}\\ \tau_{\mathbb{xy}}\end{Bmatrix}d\mathbb{z},\begin{Bmatrix}\mathbb{M}_{\mathbb{x}}\\ \mathbb{M}_{\mathbb{y}}\\ \mathbb{M}_{\mathbb{xy}}\end{Bmatrix}=\int_{-h/2}^{h/2}\mathbb{z}\begin{Bmatrix}\sigma_{\mathbb{x}}\\ \sigma_{\mathbb{y}}\\ \tau_{\mathbb{xy}}\end{Bmatrix}d\mathbb{z},\quad \begin{Bmatrix}\mathbb{Q}_{\mathbb{xz}}\\ \mathbb{Q}_{\mathbb{yz}}\end{Bmatrix}=\int_{-h/2}^{h/2}\begin{Bmatrix}\tau_{\mathbb{xz}}\\ \tau_{\mathbb{yz}}\end{Bmatrix}d\mathbb{z}. \tag{15}$$

To induce a work change by airflow pressure loading, $\delta\mathbb{V}$ may be expressed as follows:

$$\delta V=-\int_A q_{\mathbb{z}}\frac{\partial^2\mathbb{w}}{\partial\mathbb{x}^2}\delta\mathbb{w}\,dA. \tag{16}$$

In which:

$$q_{\mathbb{z}}=\frac{1}{2}\rho_{\mathrm{air}}V_{\mathrm{air}}^2\sin(\theta_{\mathrm{air}}). \tag{17}$$

in which, θ_{air} and V_{air} refer to, respectively, the wind attack angle and the average wind speed; the air density, denoted as ρ_{air}, is assumed to be $\rho_{\mathrm{air}}=1.235\ [\mathrm{kg/m^3}]$ [66].

Where θ_{air} and V_{air} stand for the wind attack angle and average wind speed, respectively; ρ_{air}, the air density, is taken to be $\rho_{\text{air}} = 1.235\ \left[\text{kg/m}^3\right]$ [66]. The following may be used to identify the component of δK:

$$\begin{aligned}\delta K &= \int_V (\dot{\mathbb{u}}\,\delta\dot{\mathbb{u}} + \dot{\nu}\delta\dot{\nu} + \dot{\mathbb{w}}\,\delta\dot{\mathbb{w}})\rho d\mathbb{V} \\ &= \int_A \left(\mathcal{I}_1\left(\frac{\partial \mathbb{u}}{\partial t}\frac{\partial \delta\mathbb{u}}{\partial t} + \frac{\partial \nu}{\partial t}\frac{\partial \delta\nu}{\partial t} + \frac{\partial \mathbb{w}}{\partial t}\frac{\partial \delta\mathbb{w}}{\partial t}\right)\right. \\ &\quad + \mathcal{I}_2\left(\frac{\partial \mathbb{u}}{\partial t}\frac{\partial \delta\varphi_{\mathbb{x}}}{\partial t} + \frac{\partial \varphi_{\mathbb{x}}}{\partial t}\frac{\partial \delta\mathbb{u}}{\partial t} + \frac{\partial \mathbb{v}}{\partial t}\frac{\partial \delta\varphi_{\mathbb{y}}}{\partial t} + \frac{\partial \varphi_{\mathbb{y}}}{\partial t}\frac{\partial \delta\nu}{\partial t}\right) \\ &\quad \left. + \mathcal{I}_3\left(\frac{\partial \varphi_{\mathbb{x}}}{\partial t}\frac{\partial \delta\varphi_{\mathbb{x}}}{\partial t} + \frac{\partial \varphi_{\mathbb{y}}}{\partial t}\frac{\partial \delta\varphi_{\mathbb{y}}}{\partial t}\right)\right) dA.\end{aligned} \tag{18}$$

The variables $(\mathcal{I}_1, \mathcal{I}_2, \mathcal{I}_3)$ serve as representations of the inertial mass components within the doubly curved panel, and the details are as follows:

$$(\mathcal{I}_1, \mathcal{I}_2, \mathcal{I}_3) = \int_{-h/2}^{h/2} \rho(1, \mathbb{z}, \mathbb{z}^2) d\mathbb{z}. \tag{19}$$

By replacing Eqs. (14), (16), and (18) into Eq. (13), we may get the governing equation of motion:

$$\delta\mathbb{u} : \frac{\partial \mathbb{N}_{\mathbb{x}}}{\partial \mathbb{x}} + \frac{\partial \mathbb{N}_{\mathbb{xy}}}{\partial \mathbb{y}} + \frac{\mathbb{Q}_{\mathbb{xz}}}{R_1} = \mathcal{I}_1\frac{\partial^2 \mathbb{u}}{\partial t^2} + \mathcal{I}_2\frac{\partial^2 \varphi_{\mathbb{x}}}{\partial t^2}, \tag{20a}$$

$$\delta\mathbb{v} : \frac{\partial \mathbb{N}_{\mathbb{y}}}{\partial \mathbb{y}} + \frac{\partial \mathbb{N}_{\mathbb{xy}}}{\partial \mathbb{x}} + \frac{\mathbb{Q}_{\mathbb{yz}}}{R_2} = \mathcal{I}_1\frac{\partial^2 \mathbb{v}}{\partial t^2} + \mathcal{I}_2\frac{\partial^2 \varphi_{\mathbb{y}}}{\partial t^2}, \tag{20b}$$

$$\delta\mathbb{w} : \frac{\partial \mathbb{Q}_{\mathbb{xz}}}{\partial \mathbb{x}} + \frac{\partial \mathbb{Q}_{\mathbb{yz}}}{\partial \mathbb{y}} - \frac{\mathbb{N}_{\mathbb{x}}}{R_1} - \frac{\mathbb{N}_{\mathbb{y}}}{R_2} - q_{\mathbb{z}} = \mathcal{I}_1\frac{\partial^2 \mathbb{w}}{\partial t^2}, \tag{20c}$$

$$\delta\varphi_{\mathbb{x}} : \frac{\partial \mathbb{M}_{\mathbb{x}}}{\partial \mathbb{x}} + \frac{\partial \mathbb{M}_{\mathbb{xy}}}{\partial \mathbb{y}} - \mathbb{Q}_{\mathbb{xz}} = \mathcal{I}_2\frac{\partial^2 \mathbb{u}}{\partial t^2} + \mathcal{I}_3\frac{\partial^2 \varphi_{\mathbb{x}}}{\partial t^2}, \tag{20d}$$

$$\delta\varphi_{\mathbb{y}} : \frac{\partial \mathbb{M}_{\mathbb{y}}}{\partial \mathbb{y}} + \frac{\partial \mathbb{M}_{\mathbb{xy}}}{\partial \mathbb{x}} - \mathbb{Q}_{\mathbb{yz}} = \mathcal{I}_2\frac{\partial^2 \mathbb{v}}{\partial t^2} + \mathcal{I}_3\frac{\partial^2 \varphi_{\mathbb{y}}}{\partial t^2}. \tag{20e}$$

in addition, through Eqs. (15) and (19), Eqs. (20a)–(20e) can be further rewritten as:

$$\begin{aligned}\delta\mathbb{u} :\ & \mathbb{A}_{11}\frac{\partial^2 \mathbb{u}}{\partial \mathbb{x}^2} + \mathbb{A}_{66}\frac{\partial^2 \mathbb{u}}{\partial \mathbb{y}^2} - \frac{\mathbb{A}_{55}\mathbb{u}}{R_1^2} + \mathbb{A}_{12}\frac{\partial^2 \mathbb{v}}{\partial \mathbb{x}\partial \mathbb{y}} + \mathbb{A}_{66}\frac{\partial^2 \mathbb{v}}{\partial \mathbb{x}\partial \mathbb{y}} \\ & + \frac{\mathbb{A}_{11}}{R_1}\frac{\partial \mathbb{w}}{\partial \mathbb{x}} + \mathbb{A}_{12}\frac{\partial \mathbb{w}}{R_2\partial \mathbb{x}} + \frac{\mathbb{A}_{55}}{R_1}\frac{\partial \mathbb{w}}{\partial \mathbb{x}} + \mathbb{B}_{11}\frac{\partial^2 \varphi_{\mathbb{x}}}{\partial \mathbb{x}^2} \\ & + \mathbb{B}_{66}\frac{\partial^2 \varphi_{\mathbb{x}}}{\partial \mathbb{y}^2} + \frac{\mathbb{A}_{55}\varphi_{\mathbb{x}}}{R_1} + \mathbb{B}_{12}\frac{\partial^2 \varphi_{\mathbb{y}}}{\partial \mathbb{x}\partial \mathbb{y}} + \mathbb{B}_{66}\frac{\partial^2 \varphi_{\mathbb{y}}}{\partial \mathbb{xy}} \\ = &\ \mathcal{I}_1\frac{\partial^2 \mathbb{u}}{\partial t^2} + \mathcal{I}_2\frac{\partial^2 \varphi_{\mathbb{x}}}{\partial t^2},\end{aligned} \tag{21a}$$

$$\begin{aligned}\delta\mathbb{v} :\ & \mathbb{A}_{12}\frac{\partial^2 \mathbb{u}}{\partial \mathbb{x}\partial \mathbb{y}} + \mathbb{A}_{66}\frac{\partial^2 \mathbb{u}}{\partial \mathbb{x}\partial \mathbb{y}} + \mathbb{A}_{22}\frac{\partial^2 \mathbb{v}}{\partial \mathbb{y}^2} + \mathbb{A}_{66}\frac{\partial^2 \mathbb{v}}{\partial \mathbb{x}^2} - \frac{\mathbb{A}_{44}\mathbb{v}}{R_2^2} \\ & + \frac{\mathbb{A}_{12}\partial \mathbb{w}}{R_1\partial \mathbb{y}} + \frac{\mathbb{A}_{22}}{R_2}\frac{\partial \mathbb{w}}{\partial \mathbb{y}} + \frac{\mathbb{A}_{44}}{R_2}\frac{\partial \mathbb{w}}{\partial \mathbb{y}} + \mathbb{B}_{12}\frac{\partial^2 \varphi_{\mathbb{x}}}{\partial \mathbb{x}\partial \mathbb{y}} \\ & + \mathbb{B}_{66}\frac{\partial^2 \varphi_{\mathbb{x}}}{\partial \mathbb{x}\partial \mathbb{y}} + \mathbb{B}_{22}\frac{\partial^2 \varphi_{\mathbb{y}}}{\partial \mathbb{y}^2} + \mathbb{B}_{66}\frac{\partial^2 \varphi_{\mathbb{y}}}{\partial \mathbb{x}^2} + \frac{\mathbb{A}_{44}\varphi_{\mathbb{y}}}{R_2} \\ = &\ \mathcal{I}_1\frac{\partial^2 \mathbb{v}}{\partial t^2} + \mathcal{I}_2\frac{\partial^2 \varphi_{\mathbb{y}}}{\partial t^2},\end{aligned} \tag{21b}$$

$$\begin{aligned}\delta\mathbb{w} :\ & -\left(\frac{(\mathbb{A}_{11} + \mathbb{A}_{55})}{R_1} + \frac{\mathbb{A}_{12}}{R_2}\right)\frac{\partial \mathbb{u}}{\partial \mathbb{x}} \\ & - \left(\frac{(\mathbb{A}_{22} + \mathbb{A}_{44})}{R_2} + \frac{\mathbb{A}_{12}}{R_1}\right)\frac{\partial \mathbb{v}}{\partial \mathbb{y}} + \left(\frac{\mathbb{A}_{11}}{R_1^2} + \frac{\mathbb{A}_{22}}{R_2^2} + \frac{2\mathbb{A}_{12}}{R_1R_2}\right)\mathbb{w} \\ & + \mathbb{A}_{55}\frac{\partial^2 \mathbb{w}}{\partial \mathbb{x}^2} + \mathbb{A}_{44}\frac{\partial^2 \mathbb{w}}{\partial \mathbb{y}^2} - q_{\mathbb{z}}\frac{\partial^2 \mathbb{w}}{\partial \mathbb{x}^2} + \mathbb{A}_{55}\frac{\partial \varphi_{\mathbb{x}}}{\partial \mathbb{x}} \\ & - \left(\frac{\mathbb{B}_{11}}{R_1} + \frac{\mathbb{B}_{12}}{R_2}\right)\frac{\partial \varphi_{\mathbb{x}}}{\partial \mathbb{x}} + \mathbb{A}_{44}\frac{\partial \varphi_{\mathbb{y}}}{\partial \mathbb{y}} - \left(\frac{\mathbb{B}_{12}}{R_1} + \frac{\mathbb{B}_{22}}{R_2}\right)\frac{\partial \varphi_{\mathbb{y}}}{\partial \mathbb{y}} \\ = &\ \mathcal{I}_1\frac{\partial^2 \mathbb{w}}{\partial t^2},\end{aligned} \tag{21c}$$

$$\begin{aligned}\delta\varphi_{\mathbb{x}} :\ & \mathbb{B}_{11}\frac{\partial^2 \mathbb{u}}{\partial \mathbb{x}^2} + \mathbb{B}_{66}\frac{\partial^2 \mathbb{u}}{\partial \mathbb{y}^2} + \frac{\mathbb{A}_{55}\mathbb{u}}{R_1} + \mathbb{B}_{12}\frac{\partial^2 \mathbb{v}}{\partial \mathbb{x}\partial \mathbb{y}} + \mathbb{B}_{66}\frac{\partial^2 \mathbb{v}}{\partial \mathbb{x}\partial \mathbb{y}} \\ & + \frac{\mathbb{B}_{11}}{R_1}\frac{\partial \mathbb{w}}{\partial \mathbb{x}} + \mathbb{B}_{12}\frac{\partial \mathbb{w}}{R_2\partial \mathbb{x}} - \mathbb{A}_{55}\frac{\partial \mathbb{w}}{\partial \mathbb{x}} + \mathbb{D}_{11}\frac{\partial^2 \varphi_{\mathbb{x}}}{\partial \mathbb{x}^2} \\ & + \mathbb{D}_{66}\frac{\partial^2 \varphi_{\mathbb{x}}}{\partial \mathbb{y}^2} - \mathbb{A}_{55}\varphi_{\mathbb{x}} + \mathbb{D}_{12}\frac{\partial^2 \varphi_{\mathbb{y}}}{\partial \mathbb{x}\partial \mathbb{y}} + \mathbb{D}_{66}\frac{\partial^2 \varphi_{\mathbb{y}}}{\partial \mathbb{x}\partial \mathbb{y}} \\ = &\ \mathcal{I}_2\frac{\partial^2 \mathbb{u}}{\partial t^2} + \mathcal{I}_3\frac{\partial^2 \varphi_{\mathbb{x}}}{\partial t^2},\end{aligned} \tag{21d}$$

$$\begin{aligned}\delta\varphi_{\mathbb{y}} :\ & \mathbb{B}_{12}\frac{\partial^2 \mathbb{u}}{\partial \mathbb{x}\partial \mathbb{y}} + \mathbb{B}_{66}\frac{\partial^2 \mathbb{u}}{\partial \mathbb{x}\partial \mathbb{y}} + \mathbb{B}_{22}\frac{\partial^2 \mathbb{v}}{\partial \mathbb{y}^2} + \mathbb{B}_{66}\frac{\partial^2 \mathbb{v}}{\partial \mathbb{x}^2} + \frac{\mathbb{A}_{44}\mathbb{v}}{R_2} \\ & + \frac{\mathbb{B}_{12}\partial \mathbb{w}}{R_1\partial \mathbb{y}} + \frac{\mathbb{B}_{22}}{R_2}\frac{\partial \mathbb{w}}{\partial \mathbb{y}} - \mathbb{A}_{44}\frac{\partial \mathbb{w}}{\partial \mathbb{y}} + \mathbb{D}_{12}\frac{\partial^2 \varphi_{\mathbb{x}}}{\partial \mathbb{x}\partial \mathbb{y}} \\ & + \mathbb{D}_{66}\frac{\partial^2 \varphi_{\mathbb{x}}}{\partial \mathbb{x}\partial \mathbb{y}} + \mathbb{D}_{22}\frac{\partial^2 \varphi_{\mathbb{y}}}{\partial \mathbb{y}^2} + \mathbb{D}_{66}\frac{\partial^2 \varphi_{\mathbb{y}}}{\partial \mathbb{x}^2} - \mathbb{A}_{44}\varphi_{\mathbb{y}} \\ = &\ \mathcal{I}_2\frac{\partial^2 \mathbb{v}}{\partial t^2} + \mathcal{I}_3\frac{\partial^2 \varphi_{\mathbb{y}}}{\partial t^2}.\end{aligned} \tag{21e}$$

in which

$$(\mathbb{A}_{ij}, \mathbb{B}_{ij}, \mathbb{D}_{ij}) = \int_{-h/2}^{h/2} Q_{ij}(1, \mathbb{z}, \mathbb{z}^2) d\mathbb{z}, (i, j = 1, 2, 6), \tag{22a}$$

$$\mathbb{A}_{ij} = \int_{-h/2}^{h/2} k_s Q_{ij} d\mathbb{z}, (i, j = 4, 5). \tag{22b}$$

where the coefficient of shear correction, k_s, has a value of 5/6. All corners of the GPLRC doubly curved panel have complete simple support, which is described as:

$$\mathbb{v} = \mathbb{w} = \phi_{\mathbb{y}} = \mathbb{N}_{\mathbb{x}} = \mathbb{M}_{\mathbb{x}} = 0 \text{ at } \mathbb{x} = 0, a. \tag{23a}$$

$$\mathbb{u} = \mathbb{w} = \phi_{\mathbb{x}} = \mathbb{N}_{\mathbb{y}} = \mathbb{M}_{\mathbb{y}} = 0 \text{ at } \mathbb{y} = 0, b. \tag{23b}$$

To meet the boundary condition, the displacement functions are then extended into a double trigonometric series using Navier's solution method:

$$\begin{Bmatrix} u(x,y,t) \\ v(x,y,t) \\ w(x,y,t) \\ \phi_{\mathbb{x}}(x,y,t) \\ \phi_{\mathbb{y}}(x,y,t) \end{Bmatrix} = \sum_{m=1}^{\mathbb{M}} \sum_{n=1}^{\mathbb{N}} \begin{Bmatrix} \mathbb{U}_{mn}(x,y) \\ \mathbb{V}_{mn}(x,y) \\ \mathbb{W}_{m}(x,y) \\ \varphi_{\mathbb{x}mn}(x,y) \\ \varphi_{\mathbb{y}mn}(x,y) \end{Bmatrix} e^{j\omega_{mn}t}$$
$$= \sum_{m=1}^{\mathbb{M}} \sum_{n=1}^{\mathbb{N}} \begin{Bmatrix} A_{mn}\cos(\alpha\mathbb{x})\sin(\beta\mathbb{y}) \\ B_{mn}\sin(\alpha\mathbb{x})\cos(\beta\mathbb{y}) \\ C_{mn}\sin(\alpha\mathbb{x})\sin(\beta\mathbb{y}) \\ D_{mn}\cos(\alpha\mathbb{x}) si(\beta\mathbb{y}) \\ E_{mn}\sin(\alpha\mathbb{x})\cos(\beta\mathbb{y}) \end{Bmatrix} e^{j\omega_{mn}t}. \tag{24}$$

The mode numbers are represented by (m, n), while $(\mathbb{M}, \mathbb{N})$ denote the corresponding truncated coefficients. In the equation, the symbol $\alpha = m\pi/a$, $\beta = n\pi/b$, $j = \sqrt{-1}$ and the modal functions are comprised of $\mathbb{U}_{mn}(\mathbb{x},\mathbb{y})$, $\mathbb{V}_{mn}(\mathbb{x},\mathbb{y})$, $\mathbb{W}_{mn}(\mathbb{x},\mathbb{y})$, $\varphi_{\mathbb{x}mn}(\mathbb{x},\mathbb{y})$, and $\varphi_{\mathbb{y}mn}(\mathbb{x},\mathbb{y})$, while A_{mn}, B_{mn}, C_{mn}, D_{mn}, and E_{mn} represent the displacement amplitudes. Equation (24) may be inserted into Eqs. (21a)–(21e) to provide the mathematical solution for the doubly curved panel's free vibration under airflow pressure as follows:

$$\begin{bmatrix} \mathcal{T}_{11} - \omega_{mn}^2 \mathcal{J}_1 & \mathcal{T}_{12} & \mathcal{T}_{13} & \mathcal{T}_{14} - \omega_{mn}^2 \mathcal{J}_2 & \mathcal{T}_{15} - \omega_{mn}^2 \mathcal{J}_2 \\ \mathcal{T}_{21} & \mathcal{T}_{22} - \omega_{mn}^2 \mathcal{J}_1 & \mathcal{T}_{23} & \mathcal{T}_{24} & \mathcal{T}_{25} \\ \mathcal{T}_{31} & \mathcal{T}_{32} & \mathcal{T}_{33} - \omega_{mn}^2 \mathcal{J}_1 & \mathcal{T}_{34} & \mathcal{T}_{35} \\ \mathcal{T}_{41} - \omega_{mn}^2 \mathcal{J}_2 & \mathcal{T}_{42} & \mathcal{T}_{43} & \mathcal{T}_{44} - \omega_{mn}^2 \mathcal{J}_3 & \mathcal{T}_{45} \\ \mathcal{T}_{51} & \mathcal{T}_{52} - \omega_{mn}^2 \mathcal{J}_2 & \mathcal{T}_{53} & \mathcal{T}_{54} & \mathcal{T}_{55} - \omega_{mn}^2 \mathcal{J}_3 \end{bmatrix} \begin{bmatrix} A_{mn} \\ B_{mn} \\ C_{mn} \\ D_{mn} \\ E_{mn} \end{bmatrix} = \begin{bmatrix} 0 \\ 0 \\ 0 \\ 0 \\ 0 \end{bmatrix}, \tag{25}$$

in which

$$\mathcal{T}_{11} = -\mathbb{A}_{11}\alpha^2 - \mathbb{A}_{66}\beta^2 - \frac{\mathbb{A}_{55}}{R_1^2}, \mathcal{T}_{12} = -\mathbb{A}_{12}\alpha\beta - \mathbb{A}_{66}\alpha\beta,$$
$$\mathcal{T}_{13} = \frac{\mathbb{A}_{11}}{R_1}\alpha + \frac{\mathbb{A}_{12}}{R_2}\alpha + \frac{\mathbb{A}_{55}}{R_1}\alpha, \tag{26a}$$

$$\mathcal{T}_{14} = -\mathbb{B}_{11}\alpha^2 - \mathbb{B}_{66}\beta^2 + \frac{\mathbb{A}_{55}}{R_1}, \mathcal{T}_{15} = -\mathbb{B}_{12}\alpha\beta - \mathbb{B}_{66}\alpha\beta,$$
$$\mathcal{T}_{21} = -\mathbb{A}_{12}\alpha\beta - \mathbb{A}_{66}\alpha\beta, \tag{26b}$$

$$\mathcal{T}_{22} = -\mathbb{A}_{22}\beta^2 - \mathbb{A}_{66}\alpha^2 - \frac{\mathbb{A}_{44}\mathbb{V}}{R_2^2},$$
$$\mathcal{T}_{23} = \frac{\mathbb{A}_{12}}{R_1}\beta + \frac{\mathbb{A}_{22}}{R_2}\beta + \frac{\mathbb{A}_{44}}{R_2}\beta, \tag{26c}$$

$$\mathcal{T}_{24} = -\mathbb{B}_{12}\alpha\beta - \mathbb{B}_{66}\alpha\beta, \mathcal{T}_{25} = -\mathbb{B}_{22}\beta^2 - \mathbb{B}_{66}\alpha^2 + \frac{\mathbb{A}_{44}}{R_{2,}} \tag{26d}$$

$$\mathcal{T}_{31} = \left(\frac{(\mathbb{A}_{11} + \mathbb{A}_{55})}{R_1} + \frac{\mathbb{A}_{12}}{R_2}\right)\alpha,$$
$$\mathcal{T}_{32} = \left(\frac{(\mathbb{A}_{22} + \mathbb{A}_{44})}{R_2} + \frac{\mathbb{A}_{12}}{R_1}\right)\beta, \tag{26e}$$

$$\mathcal{T}_{33} = \left(\frac{\mathbb{A}_{11}}{R_1^2} + \frac{\mathbb{A}_{22}}{R_2^2} + \frac{2\mathbb{A}_{12}}{R_1 R_2}\right) - \mathbb{A}_{55}\alpha^2 - \mathbb{A}_{44}\beta^2 + q_{\mathbb{z}}\alpha^2,$$
$$\mathcal{T}_{34} = -\mathbb{A}_{55}\alpha + \left(\frac{\mathbb{B}_{11}}{R_1} + \frac{\mathbb{B}_{12}}{R_2}\right)\alpha, \tag{26f}$$

$$\mathcal{T}_{35} = -\mathbb{A}_{44}\beta + \left(\frac{\mathbb{B}_{12}}{R_1} + \frac{\mathbb{B}_{22}}{R_2}\right)\beta, \mathcal{T}_{41} = -\mathbb{B}_{11}\alpha^2 - \mathbb{B}_{66}\beta^2 + \frac{\mathbb{A}_{55}}{R_{1,}} \tag{26g}$$

$$\mathcal{T}_{42} = -\mathbb{B}_{12}\alpha\beta - \mathbb{B}_{66}\alpha\beta, \mathcal{T}_{43} = \frac{\mathbb{B}_{11}}{R_1}\alpha + \frac{\mathbb{B}_{12}}{R_2}\alpha - \mathbb{A}_{55}\alpha, \tag{26h}$$

$$\mathcal{T}_{44} = -\mathbb{D}_{11}{}^2 - \mathbb{D}_{66}\beta^2 - \mathbb{A}_{55}, \mathcal{T}_{45} = -\mathbb{D}_{12}\alpha\beta - \mathbb{D}_{66}\alpha\beta, \tag{26i}$$

$$\mathcal{T}_{51} = -\mathbb{B}_{12}\alpha\beta - \mathbb{B}_{66}\alpha\beta, \mathcal{T}_{52} = -\mathbb{B}_{22}\beta^2 - \mathbb{B}_{66}\alpha^2 + \frac{\mathbb{A}_{44}}{R_{2,}} \tag{26j}$$

$$\mathcal{T}_{53} = \frac{\mathbb{B}_{12}}{R_1}\beta + \frac{\mathbb{B}_{22}}{R_2}\beta - \mathbb{A}_{44}\beta, \mathcal{T}_{54} = -\mathbb{D}_{12}\alpha\beta - \mathbb{D}_{66}\alpha\beta, \tag{26k}$$

$$\mathcal{T}_{55} = -\mathbb{D}_{22}\beta^2 - \mathbb{D}_{66}\alpha^2 - \mathbb{A}_{44.} \tag{26l}$$

The dimensionless frequency can be computed as follows:

$$\omega^* = 10 \times \omega a \sqrt{\rho_m / E_m} \tag{27}$$

4. Results and discussion

This study examines the GPLRC doubly curved panel's vibration responses under airflow pressure loading. For this aim, the matrix and reinforcement are thought to be epoxy and GPLs, respectively, whose parameters are shown in Table 1. Additionally, GPLs have a size of to ($a_{\mathrm{GPL}} = 2.5[\mu\mathrm{m}]$, $b_{\mathrm{GPL}} = 1.5[\mu\mathrm{m}]$, and $t_{\mathrm{GPL}} = 1.5[\mathrm{nm}]$) and also the number of panel layers is $N_L = 10$. In this section, the influences of various parameters on the energy absorption and frequency response of the presented GPLs reinforced car's hood under airflow pressure is presented in detail.

4.1. Validation

This table presents a comparison of natural frequencies for a shallow spherical shell, specifically the (m, n) mode shapes, between the present study and previous literature [68–71]. The mode shapes are indicated by pairs (m, n), where m and n represent the number of half-waves in the circumferential and meridional directions, respectively. For the (1, 1) mode shape, the natural frequencies range from 0.50223 (Ref. [71]) to 0.53263 (Ref. [68]). The present study reports a value of 0.52830, which is consistent with the other values but slightly higher than those in Refs. [70, 71]. For the (1, 2) mode shape, the frequencies range from 0.56276 (Ref. [71]) to 0.59041 (Ref. [68]). The present study reports a frequency of 0.58853, aligning closely with. For the (2, 1) mode shape, the frequencies range from 0.56277 (Ref. [71]) to 0.59080. The present study reports a value of 0.58853, again aligning closely with Ref. [69]. For the (2, 2) mode shape, the frequencies range from 0.65788 (Ref. [71]) to 0.68486 (Ref. [68]). The present study's value is 0.68232, aligning closely with Ref. [69]. Overall, the present study's results show good agreement with previous literature, indicating reliable calculations of natural frequencies for shallow spherical shells (Table 2).

4.2. Parametric results

Figure 3 illustrates the dimensionless frequency response (ω^*) of nanocomposite-reinforced car hoods under varying airflow velocities (V_{air}) and different weight fractions of GPLs. The graph shows four curves corresponding to GPL weight fractions of 0%, 0.1%, 0.2%, and 0.3%. The dimensionless frequency response decreases as airflow velocity increases for all GPL weight fractions. Additionally, the dimensionless frequency response at a given airflow velocity increases with higher GPL weight fractions. This indicates that GPLs enhance the stiffness and structural integrity of the nanocomposite material. The observed trends suggest that incorporating GPLs improves the performance of car hoods under high airflow velocities. The increase in dimensionless frequency response with higher GPL weight fractions indicates that GPLs effectively enhance the mechanical properties of the nanocomposite. Previous research has shown that nanomaterials such as graphene significantly improve composite materials' mechanical performance. The findings in this figure align with those studies, indicating that GPLs can enhance automotive components' mechanical performance. The enhancement of the dimensionless frequency response with higher GPL weight fractions highlights the potential of GPL-reinforced nanocomposites in automotive applications. This improvement can lead to better durability and performance of car hoods under dynamic loading conditions, such as high-speed driving. However, the study's limitations include potential differences between controlled experimental conditions and real-world scenarios. Factors such as temperature variations, material aging, and manufacturing inconsistencies could influence the performance of GPL-reinforced car hoods in practice. Future research could explore the long-term durability and environmental resistance of GPL-reinforced nanocomposites. Additionally, studies could investigate the performance of these materials under combined loading conditions, such as simultaneous aerodynamic and thermal stresses. In conclusion, increasing the GPL weight fraction in nanocomposite car hoods enhances their dimensionless frequency response under airflow pressure, suggesting a promising approach to improving the mechanical performance of automotive components using nanomaterial reinforcement.

Figure 4 illustrates the dimensionless frequency response (ω^*) of nanocomposite-reinforced car hoods under varying airflow velocities for different types of graphene platelet distributions: GPL-X, GPL-O, GPL-V, and GPL-UD. The graph shows that the dimensionless frequency response decreases as airflow velocity increases across all GPL distributions. Additionally, the frequency response is highest for GPL-X and lowest for GPL-UD at any given airflow velocity. The results indicate that different GPL distributions significantly

Table 1. Material characteristics provided by for the graphene platelet and matrix medium [67].

Material properties	Epoxy	GPL
Elasticity modulus (E) [GPa]	3	1010
Mass density (ρ) [kg/m^3]	1200	1062.5
Poisson's ratio (ν)	0.34	0.186

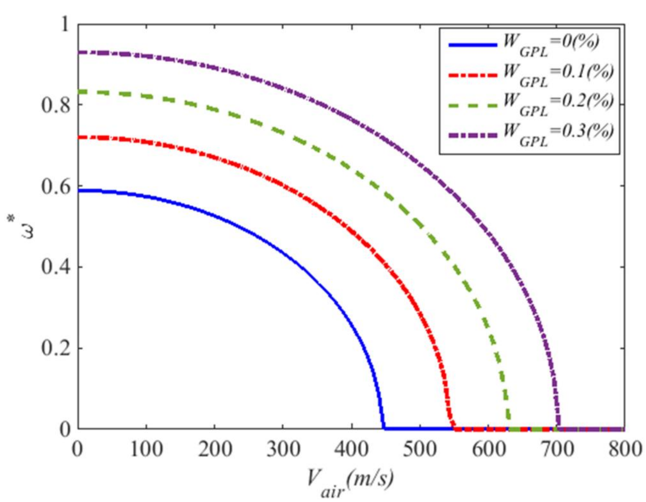

Figure 3. Dimensionless frequency response of the nanocomposites reinforced car's hood under airflow pressure for various airflow velocities and GPLs' weight fractions.

Table 2. A comparison on natural frequencies of a shallow spherical shell with those reported in literature.

(m, n)	Chern and Chao (2000) [68]	Fan and Luah (1995) [69]	Hosseini-Hashemi and Fadaee (2011) [70]	Khare et al. (2004) [71]	Present
(1, 1)	0.52543	0.53263	0.52830	0.50223	0.52830
(1, 2)	0.58420	0.59041	0.58853	0.56276	0.58853
(2, 1)	0.58427	0.59080	0.58853	0.56277	0.58853
(2, 2)	0.67676	0.68486	0.68232	0.65788	0.68232

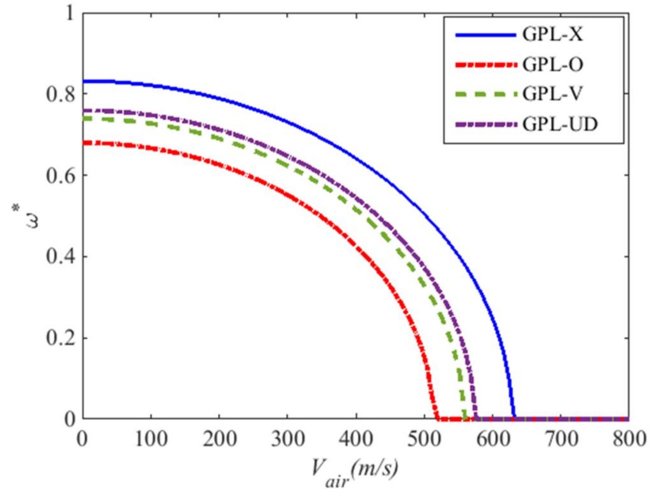

Figure 4. Dimensionless frequency response of the nanocomposites reinforced car's hood under airflow pressure for various airflow velocities and GPLs' distribution patterns.

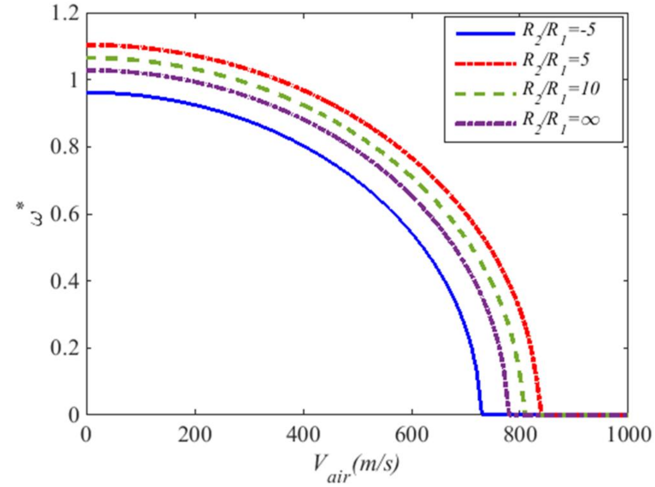

Figure 6. Dimensionless frequency response of the nanocomposites reinforced car's hood under airflow pressure for various airflow velocities and R_2/R_1 values.

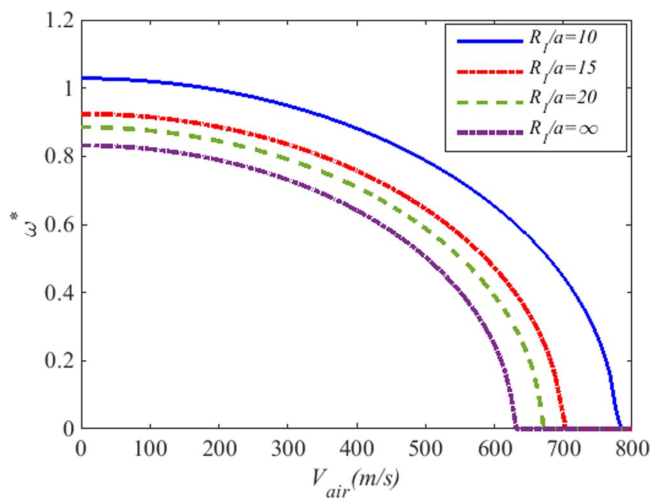

Figure 5. Dimensionless frequency response of the nanocomposites reinforced car's hood under airflow pressure for various airflow velocities and R_1/a values.

affect the mechanical properties of the nanocomposite material. GPL-X, which shows the highest dimensionless frequency response, likely enhances stiffness and structural integrity more effectively than the other distributions. Conversely, GPL-UD, with the lowest frequency response, appears to provide the least enhancement. Previous research has demonstrated that incorporating nanomaterials like graphene can improve composite materials' mechanical performance (e.g. [72]). These findings align with those studies, suggesting that specific GPL distributions can further optimize the mechanical performance of automotive components. In conclusion, the type of GPL distribution significantly influences the dimensionless frequency response of nanocomposite car hoods under airflow pressure. GPL-X shows the most significant improvement, indicating its potential for enhancing the performance of automotive components in high-speed conditions. This suggests that careful selection and optimization of GPL distributions can lead to better-performing nanocomposite materials.

Figure 5 presents the dimensionless frequency response of a nanocomposite-reinforced car hood subjected to varying airflow velocities for different ratios of R_1/a. The x-axis depicts the air velocity ranging from 0 to 800 m/s, while the y-axis shows the dimensionless frequency ranging from 0 to 1.2. The plot indicates that as the airflow velocity increases, the dimensionless frequency decreases for all R_1/a ratios. This trend is more pronounced at higher velocities, where the frequency drops significantly. For lower R_1/a values (e.g. 10 and 15), the dimensionless frequency is higher compared to higher R_1/a values (e.g. 20 and ∞) at the same air velocity. This suggests that the reinforcement effect is more substantial for smaller R_1/a ratios, enhancing the structural stiffness and thus increasing the natural frequency of the car hood. The figure effectively illustrates the relationship between airflow velocity and the dynamic response of the reinforced hood, providing insight into the performance under aerodynamic loads.

Figure 6 illustrates the dimensionless frequency response of a nanocomposite-reinforced car hood subjected to different airflow velocities for various ratios of R_2/R_1. The x-axis represents the air velocity in meters per second (m/s), ranging from 0 to 1000 m/s. The y-axis displays the dimensionless frequency, ranging from 0 to 1.2. The plot shows that as the airflow velocity increases, the dimensionless frequency decreases for all R_2/R_1 values. This decrease is more significant at higher velocities. The dimensionless frequency is generally higher for higher R_2/R_1 values (e.g. 5, 10, and ∞) compared to lower values (e.g. -5) at the same air velocity, indicating that the reinforcement effect is stronger for higher R_2/R_1 ratios. This suggests that the structural stiffness and natural frequency of the car hood increase with higher R_2/R_1 values. The figure effectively demonstrates the relationship between airflow velocity and the dynamic response of the reinforced car hood, providing valuable insights into its performance under aerodynamic loads.

Figure 7 illustrates the dimensionless frequency response of a nanocomposite-reinforced car hood subjected to different airflow velocities and varying airflow angles. The x-axis represents the air velocity in meters per second (m/s), ranging from 0 to 1000 m/s, while the y-axis shows the dimensionless

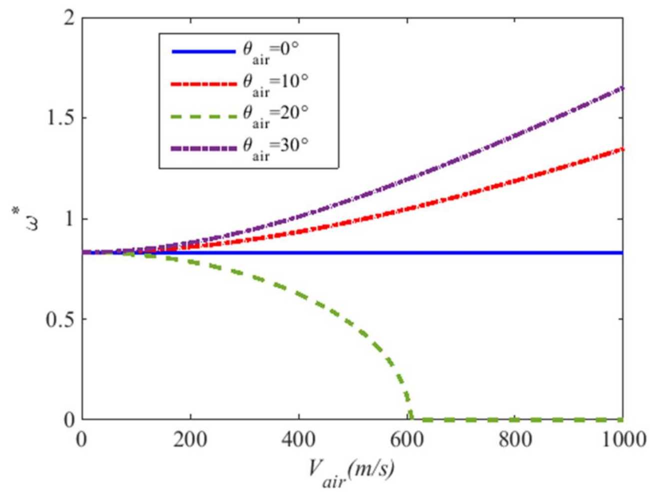

Figure 7. Dimensionless frequency response of the nanocomposites reinforced car's hood under airflow pressure for various airflow velocities and θ_{air} values.

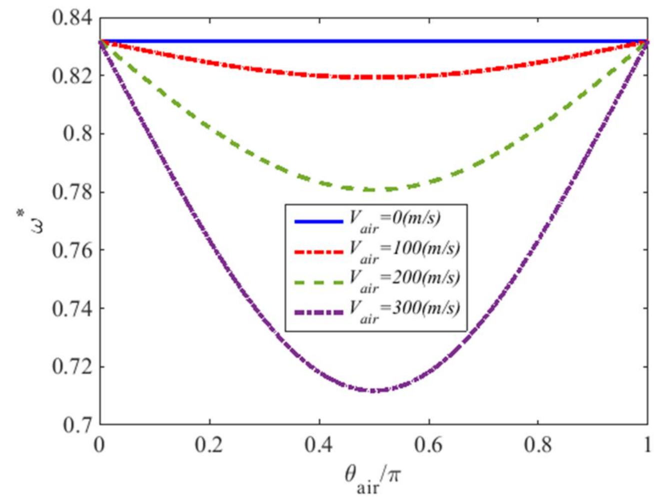

Figure 8. Dimensionless frequency response of the nanocomposites reinforced car's hood under airflow pressure for various airflow velocities and angles.

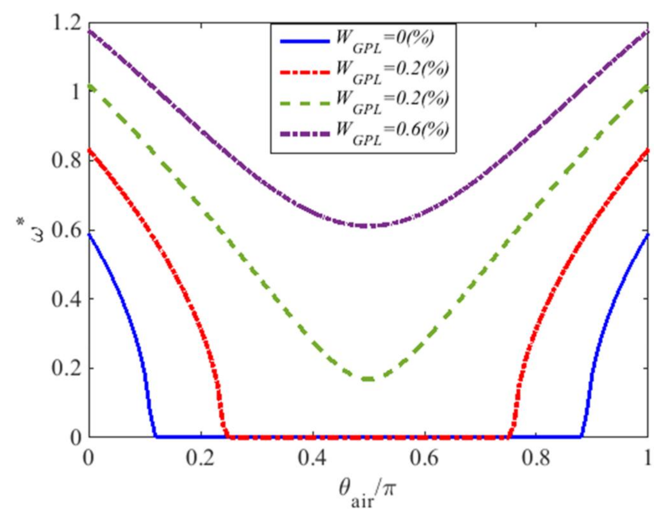

Figure 9. Dimensionless frequency response of the nanocomposites reinforced car's hood under airflow pressure for various airflow angles and GPLs' weight fraction.

frequency), ranging from 0 to 2. At $\theta_{\text{air}} = 0^{\circ}$ (blue solid line), the dimensionless frequency remains constant at approximately 1, regardless of the airflow velocity. This indicates that the frequency is unaffected by the airflow when it is perpendicular to the surface of the hood. For $\theta_{\text{air}} = 10^{\circ}$ (red dashed line), there is a slight increase in the dimensionless frequency with increasing airflow velocity, suggesting that a small incidence angle introduces some aerodynamic effects that slightly increase the natural frequency as the airflow velocity increases. The behavior at $\theta_{\text{air}} = 20^{\circ}$ (green dash-dot line) is more complex. Initially, the dimensionless frequency decreases with increasing velocity, reaching a minimum at around 600 m/s, after which it rises sharply. This indicates a more significant aerodynamic effect at this angle, causing an initial reduction in frequency followed by a rapid increase due to changing flow dynamics around the hood. For $\theta_{\text{air}} = 30^{\circ}$ (purple dotted line), the dimensionless frequency continuously increases with increasing airflow velocity. The frequency rises more steeply compared to lower angles, suggesting a strong aerodynamic influence that significantly enhances the stiffness and natural frequency of the hood at higher velocities. Overall, the figure demonstrates how varying the angle of airflow incidence impacts the dynamic response of the nanocomposite-reinforced car hood. It highlights the interplay between aerodynamic forces and structural dynamics, providing valuable insights for optimizing the hood design under different operating conditions.

Figure 8 depicts a graph representing the dimensionless frequency response of nanocomposite-reinforced car hoods under varying airflow pressures. The graph shows the relationship between the dimensionless frequency response on the y-axis and the normalized airflow angle on the x-axis. Four different curves illustrate the effect of different airflow velocities on the frequency response. The blue solid line represents the response at $V_{\text{air}} = 0\ \text{m/s}$. The curve starts at approximately 0.82, remains nearly constant across the range of airflow angles. The red dashed line corresponds to $V_{\text{air}} = 100\ \text{m/s}$. This line also starts at around 0.82 but shows a slight dip toward the center of the graph, indicating a minor decrease in frequency response with increasing airflow angle. The green dashed line represents $V_{\text{air}} = 200\ \text{m/s}$. It begins at about 0.82 but exhibits a more pronounced dip, reaching its minimum frequency response around the midpoint of the airflow angle. The purple dashed-dotted line indicates $V_{\text{air}} = 300\ \text{m/s}$. This curve starts at the same initial frequency response but shows the most significant dip, with the lowest frequency response at the center of the graph. The graph demonstrates how increasing airflow velocities cause a more substantial reduction in the frequency response, especially around the midpoint of the airflow angle. The legend is located within the graph and clearly indicates the corresponding airflow velocities for each curve.

Figure 9 presents a graph showing the dimensionless frequency response of nanocomposite-reinforced car hoods under airflow pressure for various airflow angles and different weight fractions of GPLs. The x-axis represents the normalized airflow angle, ranging from 0 to 1. The y-axis shows the dimensionless frequency response, ranging from 0 to 1.2. Four different curves are plotted to illustrate the effect of different GPL weight fractions on the frequency response: The blue solid line represents the frequency response with a GPL weight fraction of 0%. This curve starts at approximately 1.0 at both ends and dips sharply to around 0.2 at the midpoint, indicating a significant reduction in frequency response at the center of the airflow angle range. The red dashed line corresponds to $W_{\mathrm{GPL}} = 0.2\%$. This line begins at around 1.0 and also dips toward the midpoint but remains slightly higher than the blue line, indicating an improved frequency response compared to the 0% GPL case. The green dashed line represents $W_{\mathrm{GPL}} = 0.4\%$. It starts at around 1.0 and exhibits a similar dip toward the midpoint, with the minimum frequency response being higher than that of the red line, showing further improvement. The purple dashed-dotted line indicates $W_{\mathrm{GPL}} = 0.6\%$. This curve starts at about 1.0 and dips to a lesser extent than the other lines, maintaining a higher frequency response throughout the range of airflow angles. The graph highlights that increasing the GPL weight fraction results in a higher dimensionless frequency response, particularly at the midpoint of the airflow angle. The legend within the graph clearly indicates the corresponding GPL weight fractions for each curve.

Figure 10 shows dimensionless frequency response of the nanocomposites reinforced car's hood under airflow pressure for various airflow angles and GPLs' distribution patterns. The same explanation can be seen in Figure 9. According to Figure 10 can be seen that, selecting GPL-X as the GPLs' distribution pattern results in higher dimensionless natural frequency of the nanocomposites reinforced car's hood under airflow pressure for all values of airflow angle. In constant, selecting GPL-O as the GPLs' distribution pattern results in lower dimensionless natural frequency and stability of the nanocomposites reinforced car's hood under airflow pressure for all values of airflow angle. As an important outcome for related industries, for selecting GPL-O as the GPLs' distribution pattern, should have special attention to the value of airflow angle.

Figure 11 displays a plot depicting the dimensionless frequency response of nanocomposite-reinforced car hoods under airflow pressure for various airflow angles and R_1/a values. The x-axis represents the normalized airflow angle, ranging from 0 to 1, while the y-axis represents the dimensionless frequency response, ranging from 0 to 1.2. Four distinct curves, each corresponding to different R_1/a values, are shown. A solid blue line representing $R_1/a = 10$. A dashed red line representing $R_1/a = 15$. A dashed green line representing $R_1/a = 20$. A dash-dotted purple line representing $R_1/a = \infty$. The legend on the upper part of the plot identifies these lines. The graph shows a trend where the dimensionless frequency response varies with the normalized airflow angle. The response decreases to a minimum around $\theta_{\mathrm{air}}/\pi = 0.5$, and then, increases again as $\theta_{\mathrm{air}}/\pi$ approaches 1. For smaller values of $\theta_{\mathrm{air}}/\pi$ near 0 and larger values (near 1), the frequency response is higher, especially noticeable for smaller R_1/a values. The curves are closely clustered but show noticeable variations with different R_1/a values, particularly around the minimum point. The plot effectively illustrates how different R_1/a values impact the dimensionless frequency response of the nanocomposite-reinforced car hood as the airflow angle changes, highlighting the sensitivity of the dynamic behavior of the hood to both the airflow angle and the geometrical ratio.

Figure 12 displays a graph illustrating the dimensionless frequency response of nanocomposite-reinforced car hoods under airflow pressure for various airflow angles and different values of the R_2/R_1 value. The x-axis represents the normalized airflow angle, ranging from 0 to 1, while the y-axis shows the dimensionless frequency response, ranging from 0 to 1.2. Four different curves are plotted to depict the effect of different R_2/R_1 ratios on the frequency response. The blue solid line represents the frequency response with $R_2/R_1 = -5$. This curve starts at approximately 1.0 at both ends and dips sharply to around 0.1 at the midpoint, indicating a significant reduction in frequency response at the center of the airflow angle range. The red dashed line corresponds to $R_2/R_1 = 5$. This line begins at around 1.0 and

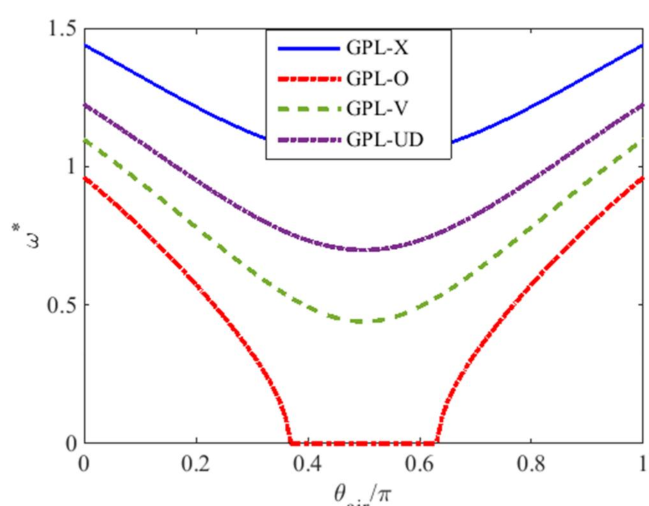

Figure 10. Dimensionless frequency response of the nanocomposites reinforced car's hood under airflow pressure for various airflow angles and GPLs' distribution patterns.

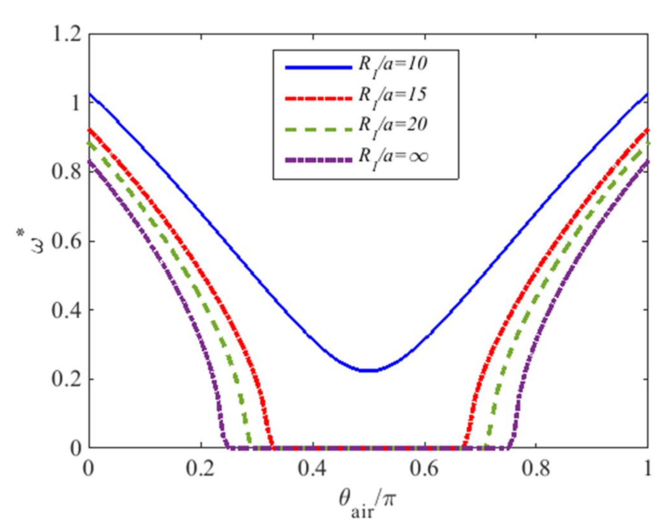

Figure 11. Dimensionless frequency response of the nanocomposites reinforced car's hood under airflow pressure for various airflow angles and R_1/a values.

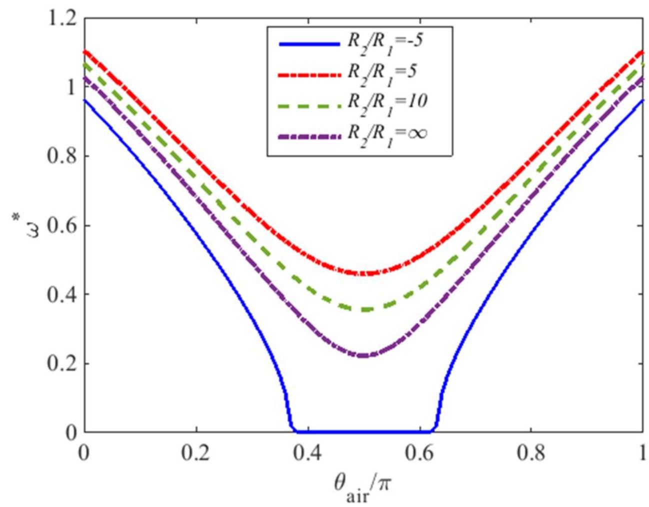

Figure 12. Dimensionless frequency response of the nanocomposites reinforced car's hood under airflow pressure for various airflow angles and R_2/R_1 values.

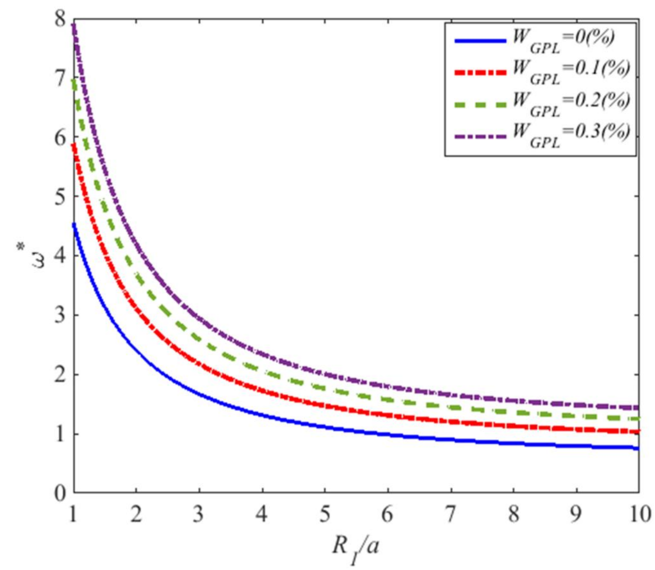

Figure 13. Dimensionless frequency response of the nanocomposites reinforced car's hood under airflow pressure for various GPLs' weight fractions and R_1/a values.

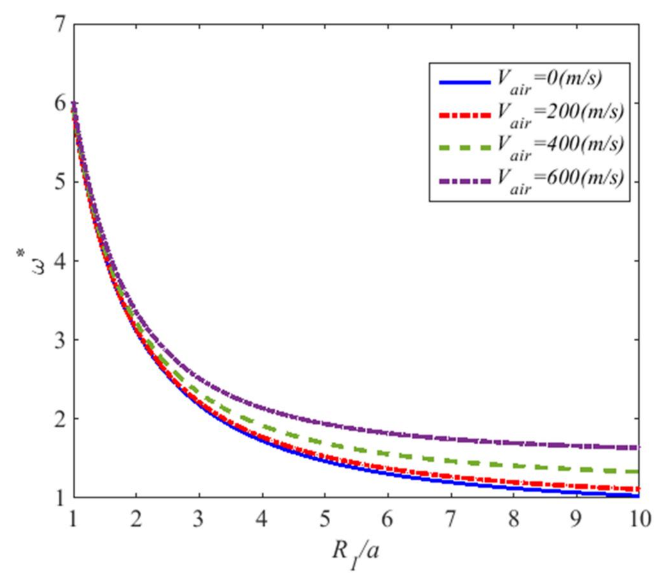

Figure 14. Dimensionless frequency response of the nanocomposites reinforced car's hood under airflow pressure for various airflow velocities and R_1/a values.

also dips toward the midpoint but remains higher than the blue line, indicating an improved frequency response compared to the −5 ratio. The green dashed line represents $R_2/R_1 = 10$. It starts at around 1.0 and exhibits a similar dip toward the midpoint, with the minimum frequency response being higher than that of the red line, showing further improvement. The purple dashed-dotted line indicates $R_2/R_1 = \infty$. This curve starts at about 1.0 and dips to a lesser extent than the other lines, maintaining a higher frequency response throughout the range of airflow angles. The graph demonstrates that increasing the R_2/R_1 ratio results in a higher dimensionless frequency response, particularly at the midpoint of the airflow angle. The legend within the graph clearly indicates the corresponding R_2/R_1 ratios for each curve.

Figure 13 illustrates a plot showing the dimensionless frequency response of nanocomposite-reinforced car hoods under airflow pressure for various graphene platelet weight fractions and R_1/a values. The x-axis represents the R_1/a ratio ranging from 1 to 10, while the y-axis displays the dimensionless frequency response ranging from 0 to 8. The plot includes four different curves, each representing a distinct GPL weight fraction. A solid blue line representing $W_{\text{GPL}} = 0\%$. A dashed red line representing $W_{\text{GPL}} = 0.1\%$. A dashed green line representing $W_{\text{GPL}} = 0.2\%$. A dash-dotted purple line representing $W_{\text{GPL}} = 0.3\%$. The legend on the right side of the plot identifies these lines. The general trend observed in the graph shows that the dimensionless frequency response decreases as R_1/a increases for all GPL weight fractions. At lower R_1/a values, the frequency response is higher, particularly for higher GPL weight fractions. The curves are closely grouped together but demonstrate noticeable variations with increasing GPL weight fractions, especially at lower R_1/a values. This indicates that higher GPL weight fractions result in a higher dimensionless frequency response across the range of R_1/a values. The plot effectively demonstrates the impact of varying GPL weight fractions on the dimensionless frequency response of the nanocomposite-reinforced car hood, highlighting the influence of GPL content on the dynamic behavior of the hood structure.

Figure 14 presents a plot depicting the dimensionless frequency response of nanocomposite-reinforced car hoods subjected to airflow pressure for various airflow velocities and R_1/a values. The x-axis represents the ratio R_1/a ranging from 1 to 10, while the y-axis shows the dimensionless frequency response ranging from 1 to 7. Four distinct curves, each corresponding to different airflow velocities, are shown. A solid blue line representing $V_{\text{air}} = 0(\text{m/s})$. A dashed red line representing $V_{\text{air}} = 200(\text{m/s})$. A dashed green line representing $V_{\text{air}} = 400(\text{m/s})$. A dash-dotted purple line representing $V_{\text{air}} = 600(\text{m/s})$. The legend on the right side of the plot clearly identifies these lines. The graph shows a general trend where the dimensionless frequency response decreases as R_1/a increases for all airflow

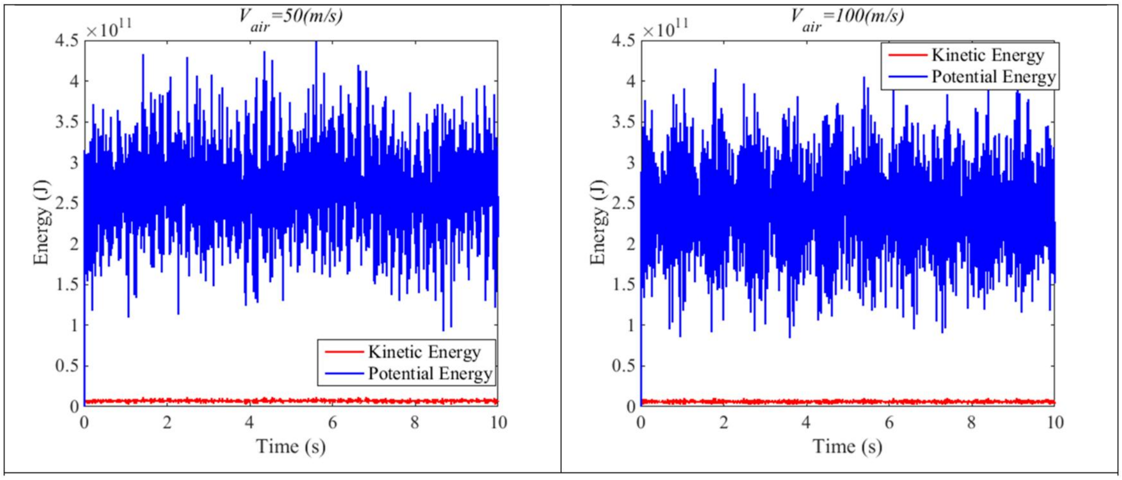

Figure 15. Energy capacity of the nanocomposites reinforced car's hood under airflow pressure for various airflow velocities.

velocities. At lower values of R_1/a, the frequency response is higher, especially noticeable for higher airflow velocities. The curves are closely clustered together but show slight variations with increasing airflow velocity, particularly noticeable at higher R_1/a values. This indicates that higher airflow velocities result in a slightly higher dimensionless frequency response across the range of R_1/a values. The plot provides a clear visual representation of how different airflow velocities affect the dimensionless frequency response of the nanocomposite-reinforced car hood, emphasizing the role of airflow in the dynamic behavior of the hood structure.

The relationship between energy absorption and natural frequency of a system is a key aspect in understanding the dynamic behavior and resilience of structures. Natural frequency refers to the rate at which a system oscillates in the absence of external forces. It is inherently tied to the system's stiffness and mass. When a system vibrates at its natural frequency, resonance can occur, potentially leading to large oscillations and higher energy absorption. Energy absorption capacity denotes the ability of a structure to dissipate energy, typically in the form of kinetic and potential energy. Structures with higher natural frequencies generally have greater stiffness, which can lead to lower deformation under dynamic loads. Conversely, structures with lower natural frequencies may absorb more energy due to greater flexibility and higher deformation. The interplay between natural frequency and energy absorption is crucial for designing systems that can withstand dynamic and impact loads. In practical terms, optimizing a structure's natural frequency can enhance its energy absorption capacity, improving its performance in applications like crashworthiness, vibration damping, and impact resistance. Effective design involves balancing these properties to achieve desired levels of energy dissipation while maintaining structural integrity and durability. Figure 15 shows the energy capacity of the nanocomposites reinforced car's hood under airflow pressure for various airflow velocities. As is seen, Kinetic energy has higher energy than Potential energy. Also, by increasing the airflow velocity, the energy capacity of the system decreases.

5. Conclusion

This study has demonstrated the significant benefits of reinforcing a car's hood with nanocomposites under airflow pressure, focusing on energy absorption and frequency analysis. The integration of nanocomposites, known for their exceptional mechanical properties, has shown to substantially enhance the energy absorption capacity and dynamic response of the hood structure. The use of advanced computational model and numerical method allowed for a detailed simulation of real-world conditions, providing robust insights into the performance improvements achieved through nanocomposite reinforcement. Our findings reveal that the nanocomposite-reinforced hood exhibits superior impact resistance and vibration dampening compared to traditional materials. This is crucial for the automotive industry, where enhancing vehicle safety and performance is of paramount importance. The improved energy absorption capacity ensures better protection of both the vehicle and its occupants during collisions, while the enhanced frequency response contributes to reduced noise, vibration, and harshness levels, leading to a more comfortable driving experience. Moreover, the dynamic performance of the hood is optimized, as the nanocomposites contribute to maintaining the structural integrity and reducing deformation under high airflow pressures. This not only improves the vehicle's overall efficiency but also enhances its stability and handling characteristics. The study underscores the potential of nanocomposite materials in advancing automotive design, particularly in developing components that are lighter, stronger, and more resilient. The research paves the way for future studies to explore the application of nanocomposites in other automotive parts, potentially revolutionizing the industry with materials that offer unparalleled performance benefits. Additionally, the methodologies employed in this study can serve as a benchmark for further investigations into the dynamic behavior of nanocomposite-reinforced structures under various loading conditions. In conclusion, the incorporation of nanocomposites in the design of car hoods presents a promising avenue for achieving significant improvements in energy absorption and frequency response.

This advancement aligns with the ongoing efforts to enhance vehicle safety, efficiency, and overall performance, making it a vital area of focus for automotive engineers and researchers.

Disclosure statement

No potential conflict of interest was reported by the author(s).

Funding

The authors extend their appreciation to King Saud University for funding this work through Researchers Supporting Project number (RSPD2024R685), King Saud University, Riyadh, Saudi Arabia.

References

[1] E. Mohseni, A.R. Saidi, and M. Mohammadi, Bending-stretching analysis of thick functionally graded micro-plates using higher-order shear and normal deformable plate theory, Mech. Adv. Mater. Struct., vol. 24, no. 14, pp. 1221–1230, 2017. DOI: 10.1080/15376494.2016.1227503.

[2] H.-S. Shen, X.-H. Huang, and J. Yang, Nonlinear bending of temperature-dependent FG-CNTRC laminated plates with negative Poisson's ratio, Mech. Adv. Mater. Struct., vol. 27, no. 13, pp. 1141–1153, 2020. DOI: 10.1080/15376494.2020.1716412.

[3] Z.-Z. Wang, T. Wang, Y.-M. Ding, and L.-S. Ma, A simple refined plate theory for the analysis of bending, buckling and free vibration of functionally graded porous plates reinforced by graphene platelets, Mech. Adv. Mater. Struct., vol. 31, no. 8, pp. 1699–1716, 2024. DOI: 10.1080/15376494.2022.2141383.

[4] A.G. Chanda and D. Punera, Porosity-dependent free vibration and transient responses of functionally graded composite plates employing higher order thickness stretching model, Mech. Adv. Mater. Struct., vol. 31, no. 7, pp. 1491–1516, 2024. DOI: 10.1080/15376494.2022.2138652.

[5] C. Lin, G. Pan, and M. Abbas, Introducing ANN-GP algorithm to estimate transient bending of the functionally graded graphene origami-enabled auxetic metamaterial structures, Mech. Adv. Mater. Struct., pp. 1–20, 2024. DOI: 10.1080/15376494.2024.2344020.

[6] J. Najd, E. Zappino, E. Carrera, W. Harizi, and Z. Aboura, Optimal position and dimensions of embedded normal piezoelectric transducers, higher order plate models and experimental approach, Mech. Adv. Mater. Struct., pp. 1–12, 2024. DOI: 10.1080/15376494.2024.2342028.

[7] E. Carrera and V.V. Zozulya, Carrera unified formulation (CUF) for the shells of revolution. Numerical evaluation, Mech. Adv. Mater. Struct., vol. 31, no. 7, pp. 1597–1619, 2024. DOI: 10.1080/15376494.2022.2140234.

[8] K. Bendine, F.B. Boukhoulda, B. Haddag, and M. Nouari, Active vibration control of composite plate with optimal placement of piezoelectric patches, Mech. Adv. Mater. Struct., vol. 26, no. 4, pp. 341–349, 2019. DOI: 10.1080/15376494.2017.1387324.

[9] M. Burkov and A. Eremin, Evaluation of fracture toughness of hybrid CNT/CFRP composites, Mech. Adv. Mater. Struct., vol. 30, no. 14, pp. 2872–2881, 2023. DOI: 10.1080/15376494.2022.2064569.

[10] A. Belounar, S. Benmebarek, and L. Belounar, Strain based triangular finite element for plate bending analysis, Mech. Adv. Mater. Struct., vol. 27, no. 8, pp. 620–632, 2020. DOI: 10.1080/15376494.2018.1488310.

[11] S.-R. Li, F. Zhang, and R.-G. Liu, Classical and homogenized expressions for the bending solutions of FGM plates based on the four variable plate theories, Mech. Adv. Mater. Struct., vol. 31, no. 15, pp. 3413–3424, 2023. DOI: 10.1080/15376494.2023.2177909.

[12] Z. Zhong, S. Chen, and E. Shang, Analytical solution of a functionally graded plate in cylindrical bending, Mech Adv Mater. Struct., vol. 17, no. 8, pp. 595–602, 2010. DOI: 10.1080/15376494.2010.517729.

[13] R. Augello, A. Pagani, and E. Carrera, Analysis of plate reinforced by straight and curved stiffeners by using novel plate elements with refined through-the-thickness expansion, Mech. Adv. Mater. Struct., pp. 1–4, 2023. DOI: 10.1080/15376494.2023.2270794.

[14] E. Carrera, M. Didem Demirbas, and R. Augello, Evaluation of stress distribution of isotropic, composite, and FG beams with different geometries in nonlinear regime via Carrera-Unified Formulation and Lagrange Polynomial Expansions, Appl. Sci., vol. 11, no. 22, pp. 10627, 2021. DOI: 10.3390/app112210627.

[15] E. Carrera, F. Miglioretti, and M. Petrolo, Accuracy of refined finite elements for laminated plate analysis, Compos. Struct., vol. 93, no. 5, pp. 1311–1327, 2011. DOI: 10.1016/j.compstruct.2010.11.007.

[16] M.M. Abdel-Mottaleb, A. Mohamed, S.A. Karim, T.A. Osman, and A. Khattab, Preparation, characterization, and mechanical properties of polyacrylonitrile (PAN)/graphene oxide (GO) nanofibers, Mech. Adv. Mater. Struct., vol. 27, no. 4, pp. 346–351, 2020. DOI: 10.1080/15376494.2018.1473535.

[17] B.W. Abuteir, E. Harkati, D. Boutagouga, S. Mamouri, and K. Djeghaba, Thermo-mechanical nonlinear transient dynamic and dynamic-buckling analysis of functionally graded material shell structures using an implicit conservative/decaying time integration scheme, Mech. Adv. Mater. Struct., vol. 29, no. 27, pp. 5773–5792, 2022. DOI: 10.1080/15376494.2021.1964115.

[18] F. Boumediene, E.M. Daya, J.-M. Cadou, and L. Duigou, Forced harmonic response of viscoelastic sandwich beams by a reduction method, Mech. Adv. Mater. Struct., vol. 23, no. 11, pp. 1290–1299, 2016. DOI: 10.1080/15376494.2015.1068408.

[19] E. Carrera, Transverse normal strain effect on thermal stress analysis of homogeneous and layered plates, AIAA J., vol. 43, no. 10, pp. 2232–2242, 2005. DOI: 10.2514/1.11230.

[20] D. Hu, H. Sun, P. Mehrabi, Y.A. Ali, and M. Al-Razgan, Application of artificial intelligence technique in optimization and prediction of the stability of the walls against wind loads in building design, Mech. Adv. Mater. Struct., vol. 31, no. 19, pp. 4755–4772, 2023. DOI: 10.1080/15376494.2023.2206208.

[21] J. Wu, Y. Yang, P. Mehrabi, and E.A. Nasr, Efficient machine-learning algorithm applied to predict the transient shock reaction of the elastic structure partially rested on the viscoelastic substrate, Mech. Adv. Mater. Struct., vol. 31, no. 16, pp. 3700–3724, 2023. DOI: 10.1080/15376494.2023.2183289.

[22] E. Carrera, A class of two-dimensional theories for anisotropic multilayered plates analysis, Atti Della Accademia Delle Scienze Di Torino. Classe Di Scienze Fisiche Matematiche e Naturali., vol. 19, pp. 1–39, 1995.

[23] M.H. Amini, M. Soleimani, A. Altafi, and A. Rastgoo, Effects of geometric nonlinearity on free and forced vibration analysis of moderately thick annular functionally graded plate, Mech. Adv. Mater. Struct., vol. 20, no. 9, pp. 709–720, 2013. DOI: 10.1080/15376494.2012.676711.

[24] A. Robaldo, E. Carrera, and A. Benjeddou, A unified formulation for finite element analysis of piezoelectric adaptive plates, Comput. Struct., vol. 84, no. 22–23, pp. 1494–1505, 2006. DOI: 10.1016/j.compstruc.2006.01.029.

[25] E. Carrera, Historical review of zig-zag theories for multilayered plates and shells, Appl. Mech. Rev., vol. 56, no. 3, pp. 287–308, 2003. DOI: 10.1115/1.1557614.

[26] E. Carrera, Developments, ideas, and evaluations based upon Reissner's mixed variational theorem in the modeling of multilayered plates and shells, Appl. Mech. Rev., vol. 54, no. 4, pp. 301–329, 2001. DOI: 10.1115/1.1385512.

[27] M. Safarpour, A. Rahimi, A. Alibeigloo, H. Bisheh, and A. Forooghi, Parametric study of three-dimensional bending and

frequency of FG-GPLRC porous circular and annular plates on different boundary conditions, Mech. Based Des. Struct. Mach., vol. 49, no. 5, pp. 707–737, 2021. DOI: 10.1080/15397734.2019.1701491.

[28] M. Safarpour, A. Forooghi, R. Dimitri, and F. Tornabene, Theoretical and numerical solution for the bending and frequency response of graphene reinforced nanocomposite rectangular plates, Appl. Sci., vol. 11, no. 14, pp. 6331, 2021. DOI: 10.3390/app11146331.

[29] M. Safarpour, and A. Alibeigloo, Elasticity solution for bending and frequency behavior of sandwich cylindrical shell with FG-CNTRC face-sheets and polymer core under initial stresses, Int. J. Appl. Mech. vol. 13, pp. 2150020, 2021. DOI: 10.1142/S1758825121500204.

[30] K. Rashvand, A. Alibeigloo, and M. Safarpour, Free vibration and instability analysis of a viscoelastic micro-shell conveying viscous fluid based on modified couple stress theory in thermal environment, Mech. Based Des. Struct. Mach., vol. 50, no. 4, pp. 1198–1236, 2022. DOI: 10.1080/15397734.2020.1745079.

[31] H. SafarPour and M. Ghadiri, Critical rotational speed, critical velocity of fluid flow and free vibration analysis of a spinning SWCNT conveying viscous fluid, Microfluid. Nanofluid., vol. 21, no. 2, pp. 1–23, 2017. DOI: 10.1007/s10404-017-1858-y.

[32] X. He, J. Ding, M. Habibi, H. Safarpour, and M. Safarpour, Non-polynomial framework for bending responses of the multi-scale hybrid laminated nanocomposite reinforced circular/annular plate, Thin-Wall. Struct., vol. 166, pp. 108019, 2021. DOI: 10.1016/j.tws.2021.108019.

[33] R. Zare, N. Najaafi, M. Habibi, F. Ebrahimi, and H. Safarpour, Influence of imperfection on the smart control frequency characteristics of a cylindrical sensor-actuator GPLRC cylindrical shell using a proportional-derivative smart controller, Smart Struct. Syst., vol. 26, no. 4, pp. 469–480, 2020.

[34] F.-Q. Su, X.-L. He, M.-J. Dai, J.-N. Yang, A. Hamanaka, Y.-H. Yu, W. Li, and J.-Y. Li, Estimation of the cavity volume in the gasification zone for underground coal gasification under different oxygen flow conditions, Energy, vol. 285, pp. 129309, 2023. DOI: 10.1016/j.energy.2023.129309.

[35] Z. Zhang, J. Chen, J. Wang, Y. Han, Z. Yu, Q. Wang, P. Zhang, and S. Yang, Effects of solder thickness on interface behavior and nanoindentation characteristics in Cu/Sn/Cu microbumps, Weld. World., vol. 66, no. 5, pp. 973–983, 2022. DOI: 10.1007/s40194-022-01261-0.

[36] Q. Gao, Z. Ding, and W.-H. Liao, Effective elastic properties of irregular auxetic structures, Compos. Struct., vol. 287, pp. 115269, 2022. DOI: 10.1016/j.compstruct.2022.115269.

[37] H. He, E. Shuang, H. Qiao, J. Yang, C. Lin, C. He, and P. Xu, A general and simple method to disperse 2D nanomaterials for promoting cement hydration, Constr. Build. Mater., vol. 427, pp. 136217, 2024. DOI: 10.1016/j.conbuildmat.2024.136217.

[38] H. Khorshidi, C. Zhang, E. Najafi, and M. Ghasemi, Fresh, mechanical and microstructural properties of alkali-activated composites incorporating nanomaterials: A comprehensive review, J. Clean. Prod., vol. 384, pp. 135390, 2022. DOI: 10.1016/j.jclepro.2022.135390.

[39] Y. Su, P.M. Iyela, J. Zhu, X. Chao, S. Kang, and X. Long, A Voronoi-based Gaussian smoothing algorithm for efficiently generating RVEs of multi-phase composites with graded aggregates and random pores, Mater. Des., vol. 244, pp. 113159, 2024. DOI: 10.1016/j.matdes.2024.113159.

[40] R. Chen, S. Wang, C. Zhang, H. Dui, Y. Zhang, Y. Zhang, and Y. Li, Component uncertainty importance measure in complex multi-state system considering epistemic uncertainties, Chin. J. Aeronaut., 2024. DOI: 10.1016/j.cja.2024.05.024.

[41] H. Zhang, Y. Xu, R. Luo, and Y. Mao, Fast GNSS acquisition algorithm based on SFFT with high noise immunity, China Commun., vol. 20, no. 5, pp. 70–83, 2023. DOI: 10.23919/JCC.2023.00.006.

[42] H. Dong, Y. Zhang, C. Yu, Z. Wang, and Y. Huang, Eco-friendly microwave absorption metastructure: Design, optimization, and performance of CPVM based on PLA@ CF, Chem. Eng. J., vol. 493, pp. 152477, 2024. DOI: 10.1016/j.cej.2024.152477.

[43] Y. Zhang, P. Zhao, Q. Lu, Y. Zhang, H. Lei, C. Yu, Y. Huang, and J. Yu, Functional additive manufacturing of large-size metastructure with efficient electromagnetic absorption and mechanical adaptation, Compos. A: Appl. Sci. Manuf., vol. 173, pp. 107652, 2023. DOI: 10.1016/j.compositesa.2023.107652.

[44] K. Ma, Y. Yu, B. Yang, and J. Yang, Demand-side energy management considering price oscillations for residential building heating and ventilation systems, IEEE Trans. Ind. Inf., vol. 15, no. 8, pp. 4742–4752, 2019. DOI: 10.1109/TII.2019.2901306.

[45] P. Zhou, R. Peng, M. Xu, V. Wu, and D. Navarro-Alarcon, Path planning with automatic seam extraction over point cloud models for robotic arc welding, IEEE Robot. Autom. Lett., vol. 6, no. 3, pp. 5002–5009, 2021. DOI: 10.1109/LRA.2021.3070828.

[46] B. Liu, H. Yang, and S. Karekal, Effect of water content on argillization of mudstone during the tunnelling process, Rock Mech. Rock Eng., vol. 53, no. 2, pp. 799–813, 2020. DOI: 10.1007/s00603-019-01947-w.

[47] H. Yang, C. Chen, J. Ni, and S. Karekal, A hyperspectral evaluation approach for quantifying salt-induced weathering of sandstone, Sci. Total Environ., vol. 885, pp. 163886, 2023. DOI: 10.1016/j.scitotenv.2023.163886.

[48] H. Yang, J. Ni, C. Chen, and Y. Chen, Weathering assessment approach for building sandstone using hyperspectral imaging technique, Herit. Sci., vol. 11, no. 1, pp. 70, 2023. DOI: 10.1186/s40494-023-00914-7.

[49] H. Yang, K. Song, and J. Zhou, Automated recognition model of geomechanical information based on operational data of tunneling boring machines, Rock Mech. Rock Eng., vol. 55, no. 3, pp. 1499–1516, 2022. DOI: 10.1007/s00603-021-02723-5.

[50] S. Han, D. Zheng, B. Mehdizadeh, E.A. Nasr, M.U. Khandaker, M. Salman, and P. Mehrabi, Sustainable design of self-consolidating green concrete with partial replacements for cement through neural-network and fuzzy technique, Sustainability, vol. 15, no. 6, pp. 4752, 2023. DOI: 10.3390/su15064752.

[51] S. Han, Z. Zhu, M. Mortazavi, A.M. El-Sherbeeny, and P. Mehrabi, Analytical assessment of the structural behavior of a specific composite floor system at elevated temperatures using a newly developed hybrid intelligence method, Buildings, vol. 13, no. 3, pp. 799, 2023. DOI: 10.3390/buildings13030799.

[52] C. Chen, H. Yang, K. Song, D. Liang, Y. Zhang, and J. Ni, Dissolution feature differences of carbonate rock within hydrofluctuation belt located in the three gorges reservoir area, Eng. Geol., vol. 327, pp. 107362, 2023. DOI: 10.1016/j.enggeo.2023.107362.

[53] K. Song, H. Yang, D. Liang, L. Chen, and M. Jaboyedoff, Steplike displacement prediction and failure mechanism analysis of slow-moving reservoir landslide, J. Hydrol., vol. 628, pp. 130588, 2024. DOI: 10.1016/j.jhydrol.2023.130588.

[54] E. Taheri, P. Mehrabi, S. Rafiei, and B. Samali, Numerical evaluation of the upright columns with partial reinforcement along with the utilisation of neural networks with combining feature-selection method to predict the load and displacement, Appl. Sci., vol. 11, no. 22, pp. 11056, 2021. DOI: 10.3390/app112211056.

[55] J. Liu, M. Mohammadi, Y. Zhan, P. Zheng, M. Rashidi, and P. Mehrabi, Utilizing artificial intelligence to predict the superplasticizer demand of self-consolidating concrete incorporating pumice, slag, and fly ash powders, Materials, vol. 14, no. 22, pp. 6792, 2021. DOI: 10.3390/ma14226792.

[56] Y. Feng, M. Mohammadi, L. Wang, M. Rashidi, and P. Mehrabi, Application of artificial intelligence to evaluate the fresh properties of self-consolidating concrete, Materials, vol. 14, no. 17, pp. 4885, 2021. DOI: 10.3390/ma14174885.

[57] E. Taheri, A. Firouzianhaji, P. Mehrabi, B. Vosough Hosseini, and B. Samali, Experimental and numerical investigation of a method for strengthening cold-formed steel profiles in bending,

Appl. Sci., vol. 10, no. 11, pp. 3855, 2020. DOI: 10.3390/app10113855.

[58] A. Firouzianhaji, N. Usefi, B. Samali, and P. Mehrabi, Shake table testing of standard cold-formed steel storage rack, Appl. Sci., vol. 11, no. 4, pp. 1821, 2021. DOI: 10.3390/app11041821.

[59] P. Mehrabi, S. Honarbari, S. Rafiei, S. Jahandari, and M. Alizadeh Bidgoli, Seismic response prediction of FRC rectangular columns using intelligent fuzzy-based hybrid metaheuristic techniques, J. Ambient Intell. Humaniz. Comput., vol. 12, no. 11, pp. 10105–10123, 2021. DOI: 10.1007/s12652-020-02776-4.

[60] E. Taheri, A. Firouzianhaji, N. Usefi, P. Mehrabi, H. Ronagh, and B. Samali, Investigation of a method for strengthening perforated cold-formed steel profiles under compression loads, Appl. Sci., vol. 9, no. 23, pp. 5085, 2019. DOI: 10.3390/app9235085.

[61] P. Mehrabi, M. Shariati, K. Kabirifar, M. Jarrah, H. Rasekh, N.T. Trung, A. Shariati, and S. Jahandari, Effect of pumice powder and nano-clay on the strength and permeability of fiber-reinforced pervious concrete incorporating recycled concrete aggregate, Constr. Build. Mater., vol. 287, pp. 122652, 2021. DOI: 10.1016/j.conbuildmat.2021.122652.

[62] A. Toghroli, P. Mehrabi, M. Shariati, N.T. Trung, S. Jahandari, and H. Rasekh, Evaluating the use of recycled concrete aggregate and pozzolanic additives in fiber-reinforced pervious concrete with industrial and recycled fibers, Constr. Build. Mater., vol. 252, pp. 118997, 2020. DOI: 10.1016/j.conbuildmat.2020.118997.

[63] H. Safarpour, K. Mohammadi, and M. Ghadiri, Temperature-dependent vibration analysis of a FG viscoelastic cylindrical microshell under various thermal distribution via modified length scale parameter: A numerical solution, J. Mech. Behav. Mater., vol. 26, no. 1–2, pp. 9–24, 2017. DOI: 10.1515/jmbm-2017-0010.

[64] J.C. Halpin Affdl and J.L. Kardos, The Halpin-Tsai equations: A review, Polym. Eng. Sci., vol. 16, no. 5, pp. 344–352, 1976. DOI: 10.1002/pen.760160512.

[65] J.N. Reddy, Mechanics of Laminated Composite Plates and Shells: Theory and Analysis, CRC Press, 2003.

[66] N.V. Nguyen, K.Q. Tran, D.T.T. Do, C.H. Thai, K.K. Żur, and H. Nguyen-Xuan, An isogeometric analysis of solar panels with a bio-inspired substrate, Eng. Anal. Bound. Elem., vol. 166, pp. 105854, 2024.

[67] H. Wu, J. Yang, and S. Kitipornchai, Parametric instability of thermo-mechanically loaded functionally graded graphene reinforced nanocomposite plates, Int. J. Mech. Sci., vol. 135, no. January, pp. 431–440, 2018.

[68] Y.-C. Chern and C.C. Chao, Comparison of natural frequencies of laminates by 3-D theory, part II: Curved panels, J. Sound Vib., vol. 230, no. 5, pp. 1009–1030, 2000. DOI: 10.1006/jsvi.1999.2454.

[69] S.C. Fan and M.H. Luah, Free vibration analysis of arbitrary thin shell structures by using spline finite element, J. Sound Vib., vol. 179, no. 5, pp. 763–776, 1995. DOI: 10.1006/jsvi.1995.0051.

[70] S. Hosseini-Hashemi and M. Fadaee, On the free vibration of moderately thick spherical shell panel—A new exact closed-form procedure, J. Sound Vib., vol. 330, no. 17, pp. 4352–4367, 2011. DOI: 10.1016/j.jsv.2011.04.011.

[71] R.K. Khare, T. Kant, and A.K. Garg, Free vibration of composite and sandwich laminates with a higher-order facet shell element, Compos. Struct., vol. 65, no. 3–4, pp. 405–418, 2004. DOI: 10.1016/j.compstruct.2003.12.003.

[72] Y. Wang, C. Feng, C. Santiuste, Z. Zhao, and J. Yang, Buckling and postbuckling of dielectric composite beam reinforced with graphene platelets (GPLs), Aerosp. Sci. Technol., vol. 91, pp. 208–218, 2019. DOI: 10.1016/j.ast.2019.05.008.